

Classical and quantum regression analysis for the optoelectronic performance of NTCDA/p-Si UV photodiode

Ahmed M. El-Mahalawy^{1,*}, and Kareem H. El-Safty^{2, **}

1. Thin Film Laboratory, Physics Department, Faculty of Science, Suez Canal University, Ismailia, Egypt.

2. Artificial Intelligence Department, DevisionX, Cairo, Egypt.

Abstract

Due to the pivotal role of UV photodiodes in many technological applications in tandem with the high efficiency achieved by machine learning techniques in regression and classification problems, different artificial intelligence (AI) techniques are adopted to simulate and model the performance of organic/inorganic heterojunction UV photodiode. Herein, the performance of a fabricated Au/NTCDA/p-Si/Al photodiode was explained in details and showed an excellent responsivity, and detectivity for UV light of intensities ranges from 20 to 80 mW/cm². A linear current–irradiance relationship was exhibited by the fabricated photodiodes under illumination up to 65 mW/cm². It also exhibits good response times of $t_{rise} = 408$ ms and $t_{fall} = 490$ ms. Furthermore, we have not only fitted the characteristic I-V curve at the highlighted intensities but also evaluated three classical algorithms; k-nearest neighbour (KNN), artificial neural network (ANN), and genetic programming (GP) besides using a quantum neural network (QNN) to predict the behaviour of the fabricated device inside and outside the studied illumination intensity range. The ANN method achieved the highest accuracy under dark and illumination conditions with a mean squared error $\sim 1.6812 \times 10^{-11}$ on the testing data. On the other hand, the Continuous-Variable (CV) QNN – using only one Qumode – has been used for the first time to model the performance of the fabricated photodiode and achieved an acceptable result with the lowest parameter set. Besides, we have utilised the full space of only one Qumode for encoding the two features using the Displaced Squeezed state preparation routine.

Keywords: Organic semiconductor – Heterojunction photodiode – Machine Learning – Genetic programming – Quantum machine learning.

*Corresponding author.

E-mail address: ahmed_elsayed@science.suez.edu.eg (A.M. El-Mahalawy)
ahmed_el.mahalawy@yahoo.com.

**Corresponding author.

E-mail address: k.elsafty@devisionx.com (Kareem H. El-Safty)
kareemessafty@gmail.com.

Contents

1	Introduction	2
2	Experimental work.....	3
2.1	Materials of the architecture and the photodiode fabrication process	3
2.2	Characterization techniques	4
2.3	Modeling procedures	4
2.3.1	Data inspection	4
2.3.2	Model selection	6
2.3.3	Artificial Neural Network (ANN)	8

2.3.4	Automated machine learning using Genetic programming.....	11
2.3.5	Quantum neural network (QNN).....	12
3	Results and Discussion.....	16
3.1	Optical Characteristics of NTCDA Thin Film	16
3.2	Electrical Characteristics of Au/NTCDA/p-Si/Al Photodiode.....	17
3.3	Optoelectronic Characteristics of Au/NTCDA/p-Si/Al Photodiode	21
3.4	Modeling the Optoelectronic Characteristics of Au/NTCDA/p-Si/Al Photodiode	26
4	Conclusion.....	30

1 Introduction

Over the past years, the technology of optoelectronic devices based on planar organic semiconductor has witnessed an escalating pace both in academia and industry. Notably, the fusion of both organic and inorganic materials to form the hybrid heterojunction devices has triggered a stir in the field of photodiode fabrication research because of their capability of tuning the spectral range of detection by changing the deposited organic film on the inorganic substrate [1].

From the multiple choices of planar structured organic materials, naphthalene tetracarboxylic dianhydride (NTCDA) has its favourable features. 1,4,5,8-naphthalene tetracarboxylic-dianhydride with a planar π -stacking structure has emerged as a promising n-type organic semiconductor material for the organic electronics community. Recently, there were several studies concerning the explanation of many physical and chemical aspects of this compound such as the degradation mechanism, hybrid complexation with inorganics and properties of monolayers epitaxial grown [2–6]. Furthermore, the unique characteristics of NTCDA such as the high electron mobility [7,8], the high UV absorption [9,10], high air stability [7,11] and the obvious photocurrent multiplication in optical photodiodes [12,13] suggest this material for a wide range of optoelectronic applications. In this framework, NTCDA was utilised in various microelectronics and optoelectronic applications such as organic light-emitting diodes (OLEDs) [14], organic photodiodes [15–17], organic solar cells (OSCs) [18,19], organic diodes [20] and n-channel organic field-effect transistor's (OFETs) [11,21–23]. According to the features mentioned above of NTCDA, the present study introduces a hybrid heterojunction based on NTCDA/p-Si for photodetection applications.

From another side, for decades, modelling techniques which depend mainly on fitting criteria have been used in physics. Lately, more sophisticated approaches have been adopted to

replace the fitting methods in computational physics. The work mentioned in references [24–29] proves that the field of Artificial Intelligence (AI) and especially Machine Learning (ML) achieved high efficiency in modelling and fitting problems in multidiscipline areas. This is considered as a vital tool which transforms the way we treat and synthesise new materials. ML models; either straightforward algorithms or Deep Learning (DL) algorithms do not only fit the data but also can predict the behaviour of microelectronic devices and give us an intuition behind the inner workings of physical phenomenon. In a retrospective manner, the relationship between condensed matter physics and ML can be exploited by the mutual benefits of using the concepts of each one to boost the progress of the other. Examples for this are the emergence of Quantum Machine Learning (QML) to improve the speed of some algorithms further and achieve higher accuracies, and using ML for discovering new materials or optimising the manufacturing process for these ones.

The present study introduces the utilisation of four different ML algorithms to model the behaviour of a fabricated hybrid heterojunction UV photodiode. The approach for the modelling part is based on Regression Analysis. This means that we no longer look for the lowest error rate but for a model that can generalise well enough to predict the behaviour of the photodiode and also can be used by others to conduct their own studies without the need of repeating the costly manufacturing process. The algorithms are divided into two main groups; classical algorithms such as KNN and Neural Networks, and quantum algorithms such as Continuous Variable (CV) Quantum Neural Networks (QNN).

2 Experimental work

2.1 Materials of the architecture and the photodiode fabrication process

The architectural design of the fabricated photodiode is illustrated in Fig.1.a, where the p-type silicon substrates were carefully etched and cleaned as mentioned in our previous work [30]. The chemical structure of 1,4,5,8-naphthalene tetracarboxylic-dianhydride, NTCDA, ($C_{14}H_4O_6$) powder purchased from *Alfa Aeser* Company is shown in the Fig.1.b. A thermally evaporated thin film of NTCDA of thickness 150 nm was deposited using the coating unit (model: Edwards 306A-England) at 1×10^{-5} mbar and room temperature. Then, a 50 nm-thick gold top electrode was deposited on NTCDA thin film using a shadow mask in the form of a

mesh. Finally, a thick aluminium bottom electrode of thickness 300 nm was deposited on the backside of Si-substrate.

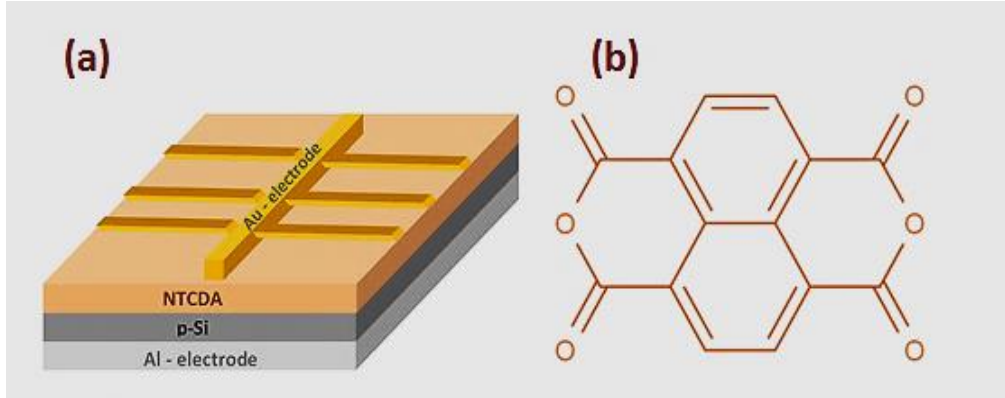


Fig.1: (a) Architecture of the fabricated photodiode, and (b) the molecular structure of NTCDA.

2.2 Characterisation techniques

The optical absorbance of NTCDA thin film on a quartz substrate was measured at normal incidence of the light at room temperature in the spectral range of 190–2500 nm using a double beam spectrophotometer (JASCO model V-570 UV-VIS-NIR). The Photoelectrical properties of the fabricated Au/NTCDA/p-Si/Al photodiode were investigated by measuring the *I-V* characteristic curve at room temperature from -3.5 V to +3.5 V using Keithley electrometer model 6517B under the influence of UV light of wavelength 194 nm. The intensity of incident light was measured using Radiometer / Photometer model IL1400A.

2.3 Modelling procedures

2.3.1 Data inspection

The approach for this section is entirely data-driven and is built on publicly available software. The chosen programming environment is Python 3.6; due to its flexibility and ease of use. We also adopted the standard pipeline for machine learning which consists of:

- I. Data acquisition.
- II. Data cleansing.
- III. Feature Engineering and pre-processing.
- IV. Model selection.
- V. Hyperparameter tuning.
- VI. Validation and testing.

In our case, the first two steps have been done using Keithley electrometer model 6517B. To decide what feature pre-processing method should be used, we must conduct an explanatory data analysis (EDA) approach; so that we can summarise the characteristics and the insights of the dataset. Based on dataset characteristics that are represented in table.1, one can speculate about the model and its properties and then find a suitable range of parameters to tune the model against a fitness function to have the optimum set of values for it. Finally, the model can be validated and tested against out of sample data.

Table.1: The estimated statistical parameters of the training and testing data.

Stats	V (Volt)	Illumination Intensity (mW/cm ²)	I (A)
No. Samples	8.28×10^2	8.28×10^2	8.28×10^2
Mean	-0.050	4.17×10^1	7.1×10^{-5}
Std	2.018	2.69×10^1	2.87×10^{-4}
Min	-3.500	0	-3.23×10^{-4}
Max	3.400	8.00×10^1	10.77×10^{-4}
25%	-1.800	2.00×10^1	-1.11×10^{-4}
50%	-0.075	4.25×10^1	2.00×10^{-6}
75%	1.700	6.50×10^1	1.33×10^{-4}

In table.1, most of the essential statistics have been summed up. The dataset consists of 828 samples and three attributes; the first two attributes are the predictors and the 3rd one – which is current – is the response. Due to the vast differences between the first two features, the interquartile range (IQR) method has been chosen to scale the features before using them.

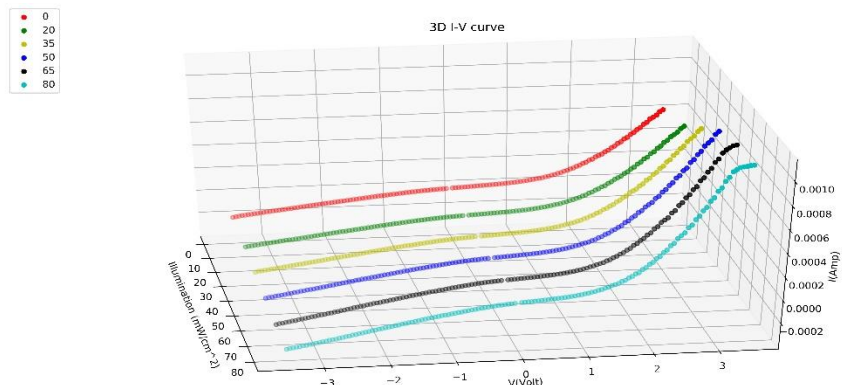


Fig.2: 3D representation for I - V characteristic curve of NTCDA/p-Si photodiode under different illumination intensities.

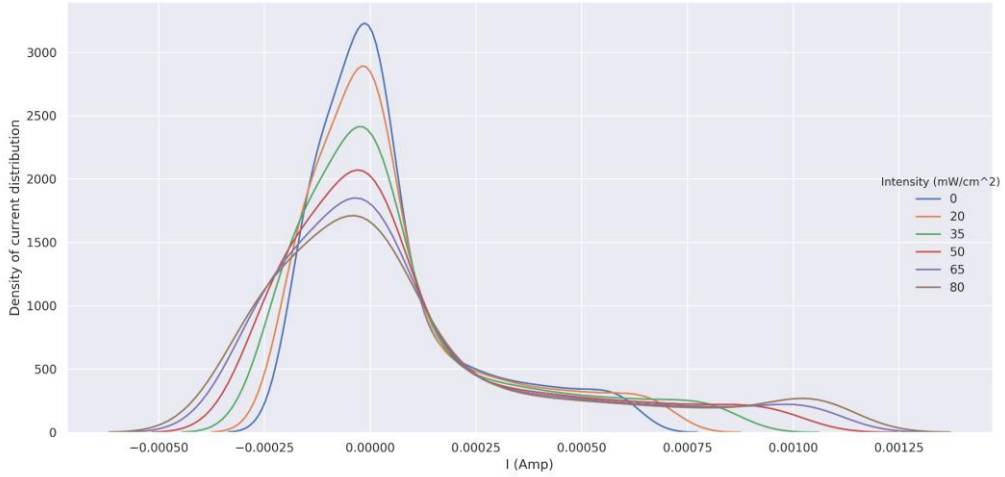


Fig.3: The current's kernel distribution based on its corresponding illumination.

From Fig.2 and Fig.3, one can assume that despite the strong correlation between the voltage and the resulted current, the illumination intensity does affect the current distribution and hence there is a nonlinear relationship between the current and the illumination. Moreover, Fig.3 represents the kernel distribution of the obtained values of the current at different illuminating intensities and confirms the nonlinear relation between them. Moreover, upon increasing the illumination intensity, the distribution function becomes broader. The obvious left-skewness is a typical asset of the organic/inorganic heterojunction devices. The absence of the sudden change in the positive side of the current distribution and smooth distribution at 50 mW/cm² confirms that the fabricated device shows its optimal performance at this illuminating intensity.

2.3.2 Model selection

For the model selection step, different types of regression models [31] have been examined and they are divided into two main groups; parametric models (i.e. linear [32,33], polynomial [34], ridge [35,36] and lasso [37]) and nonparametric models (K-nearest neighbour (KNN) [38–40], random forest [41–43] and support vector regression (SVR)[44,45], except for linear and polynomial kernels).

Herein, the parametric models are not a proper choice in the current regression problem, where the linear regression model is expressed as:

$$Y = \omega_0 + \omega_l X, \quad (1)$$

where Y and X are dependent and independent variables of a 1D vector $\in \mathbb{R}$, respectively, while ω_0 and ω_1 are the intercept and the slope of the straight line which fits the experimental data, respectively. Using a Least Squares Error method, the values of the intercept and the slope can be calculated as follows:

$$\omega_1 = \frac{\text{Cov}(X, Y)}{\text{Var}(X)} = \frac{\sum_{i=1}^n (x_i - \bar{x})(y_i - \bar{y})}{\sum_{i=1}^n (x_i - \bar{x})^2}, \quad (2)$$

$$\omega_0 = \bar{y} - \omega_1 \bar{x}, \quad (3)$$

where \bar{x} and \bar{y} are the mean of the predictor and the response variable respectively, while n is the number of the samples. For a regression problem, a closed-form solution can be used to generalise Eq (1) to be:

$$\omega = (X^T X)^{-1} X^T Y, \quad (4)$$

where X is an $m \times n$ matrix, and Y is a vector of size $m \times 1$. From Eq (1) and (4), it is evident that the linear model assumes a linear relationship between the dependent and the independent variables, and also it assumes a homoscedastic pattern in the response variable. These two properties alone clarify why a linear model is not a proper choice for modelling diode behaviour.

It is clear now to tell the difference between parametric and nonparametric [39] models which is non-parametric models do not assume a pre-determined shape or form of the independent and the dependent variables. Instead, it learns the structure of the data itself.

Moreover, a parametric model is described by a finite set of parameters, unlike any nonparametric model whose complexity depends mainly on the feature space of the dataset. Hence, according to the nonlinearity and the limited size of our dataset, nonparametric regression models are more convenient.

A KNN [38,46,47] model is chosen to be the fitting model because; it does not assume an explicit form for the training data. Moreover, despite being a nonparametric method, one can easily understand the underlying maths as well as the suitability of the feature size to the nature of KNN algorithm, where the testing time for such a model is $O(NK + Nd)$ [48] where N is the number of samples (828), d is the number of features (voltage and illumination intensity), and K is the number of the closest points to the query testing sample.

The intuition behind the Nearest Neighbour algorithm is that similar samples should have similar outputs, i.e. it follows a distance metric approach to predict the value of the next sample. The KNN is just the general variant where K is the local number of samples which could be similar to the new value that we want to predict. The algorithm uses an inverse distance weighted average of the K nearest neighbours. There are different metrics, but the most general one is the Minkowski distance metric which is defined by the following equation:

$(\sum_{i=1}^n |x_i - y_i|^p)^{\frac{1}{p}}$ where $x, y \in \mathbb{R}^2$. Furthermore, depending on the p value, one can choose between the Euclidean, Manhattan, and Chebyshev metrics.

For hyper-parameter tuning, an exhaustive grid search technique was chosen for selecting the best K value, the distance metric and its corresponding p value, and the underlying algorithm that is used for calculating the distances such as K-D Tree, Ball Tree and Brute Force [49,50], based on a cross-validation score of 13-folds. The fitness function for the grid search is the mean squared error metric. The R^2 score [51] is also evaluated to check for the goodness of the fit.

Although, the aforementioned approach, as will be discussed in the results section, achieves a great job in fitting the I - V data and reached an acceptable minimum error rate. However, our hopeful aim to obtain a lower error rate rather than that resulted from the KNN is still needed. Hence, another approach was adopted.

2.3.3 Artificial Neural Network (ANN)

The second modelling technique in the classical approach is ANN [52,53]. ANN consists of small units called neurons which act as the neurons inside our brains. As shown in Fig.4, one can formulate an equation that can describe it as follows:

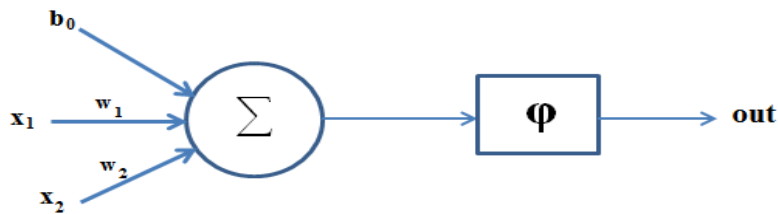


Fig.4: The working mechanism of a single neuron “perceptron”.

$$y = \varphi(w \cdot x + b), \quad (5)$$

where y is the output, w is the weight, x is a training point, b is the bias, and φ is the activation function [54,55]. According to the universality theory [53,56,57], using connected layers made of neurons enables us to approximate any known function and fit its data. An example of such a network is a multilayer perceptron or feedforward neural network as depicted in Fig.5 consists of an input layer, an output layer, and more than one hidden layer. The size of the input and the output layers depends on the problem definition which – in our case – is two neurons and one neuron, respectively. Determining the size of the hidden layers and the neurons in each one of them is still an open debate [53,58–60]. Hence, we empirically chose those numbers; starting from a shallow network with a small number of units towards the current shape depicted in Fig.6.

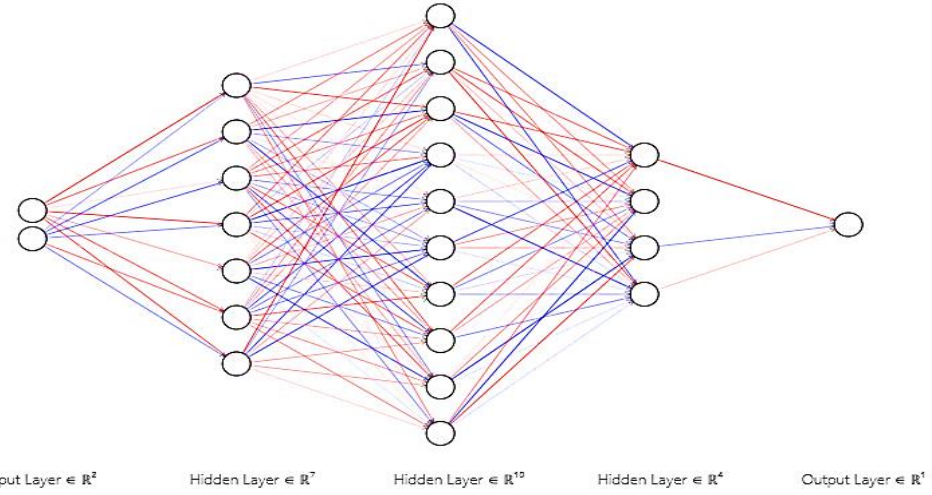


Fig.5: Feedforward neural network architecture, where the faint colours indicate extremely low weights.

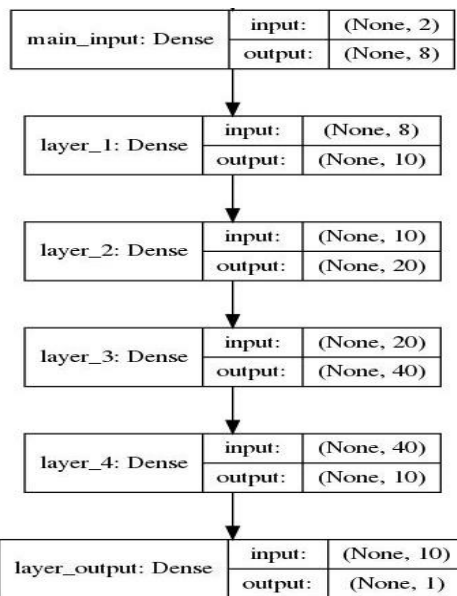


Fig.6: The configuration of the neural network (NN).

In order for a neural network to learn, it needs to be fed with data; so that it can propagate it through the layers till the output layer. After that, a feedback mechanism which is called backpropagation [61,62] is used to update the weights of each layer depending on the optimiser updating rule. Starting from the feedforward step, the output from a neuron is just its activation's output, i.e. for an input x_n where n is the number of that layer there would be an output vector y_n which would be the input of $n+1$ layer as follows:

$$\left. \begin{array}{l} y_n = f(x_n) \\ x_{n+1} = w_n \cdot y_n \end{array} \right\} \quad (6)$$

where the f is the nonlinear activation function, and w is the weight matrix between n and $n+1$ layers. Setting $n = 1$ to be the first layer and N to be the last layer, we can then move to the next step which backpropagation. Let us first define a cost function “mean squared error”:

$$E(X, W) = \frac{1}{m} \sum_{i=0}^m (y_i - w_i \cdot x_i)^2, \quad (7)$$

the error at the last layer is:

$$\delta_N = \frac{\partial E}{\partial x_N}, \quad (8)$$

and the error at the n^{th} layer is:

$$\begin{aligned} \delta_n &= \frac{\partial E}{\partial x_n} \\ &= \frac{\partial E}{\partial x_{n+1}} \frac{\partial x_{n+1}}{\partial x_n}, \end{aligned} \quad (9)$$

using Eq (6), we can formulate a relation that describes how it is possible to propagate the errors backwards through the layers for each neuron as follows:

$$\begin{aligned} \delta_n &= \delta_{n+1} \frac{\partial w_n y_n}{\partial y_n} \frac{\partial f(x_n)}{\partial x_n}, \\ &= \delta_{n+1} w_n f'(x_n) \end{aligned} \quad (10)$$

Intuitively, the error at the last layer is just the cost function multiplied by the derivative of the activation function. Finally, the third step takes care of updating the weights matrix according to the derivative between the cost function and the weights. This procedure is repeated until convergence occurs.

The updates of the weights matrix are calculated using Adam optimiser [63]. The activation function for all the layers except the last one is the RELU function [64]. The output layer's activation function is linear. The default parameters in Keras [65] of Adam's learning rate and also the weight initialisation are left unchanged. Features are usually normalised between 1 and -1 before feeding them to the network. However, we have scaled them according to their mean and standard deviation, and that helped with making convergence time a little shorter. To overcome the difficulties of the previous two approaches, a more automated approach can help to decrease the time of data inspection, feature pre-processing and model selection. Hence, an Automated Machine Learning technique is adopted [66].

2.3.4 Automated machine learning using Genetic programming

Because of the previous reasons, an automated approach is used to find the best fit that can infer the most accurate model for the prepared device. Tree-based Pipeline Optimisation Tool (TPOT) [67] is an automated machine learning library that depends on Genetic Programming [68] which is a well-known technique in Evolutionary Algorithms [69,70]. TPOT does the tedious job of pre-processing the data, feature engineering, model selection, hyper-parameter tuning, validation and finally testing. The idea lies in creating multiple copies of the dataset and feeding it to different pipelines in a tree-fashion way. It follows a simple procedure as follows [68]:

1. The initialisation of population, randomly, to be the first generation.
2. Evaluation of the cost – fitness – function to check for the best individuals.
3. Repeating the same procedure again but with some restriction parameters such as time, mutation, crossover, and selection criteria to dump the weakest individuals and breed a new generation “the offspring”.

The problem behind this approach is that in each run a new pipeline can be produced; that is why we had it run for several times, and the only thing we needed is to test each one to see if it is a good fit for our case. The chosen pipeline of this approach performs very well in terms of extrapolating unseen data and also has an acceptable error rate. Moreover, it used the same regressor method that has been chosen for the first method. The big drawback was that it produced overfitted pipelines so that we had to pay careful attention to the value of the number of cross-validations and also to the number of population size. Further details are present in the results section.

The resulted pipeline as shown in Fig.7 has three stages; the first one is modifying the data by copying it and adding a new predicted value by the XGBoost regressor [71], the second one is a feature union between the first stage and the data itself so that we have five features instead of two, the third stage is the estimator itself which is a KNN for the final prediction.

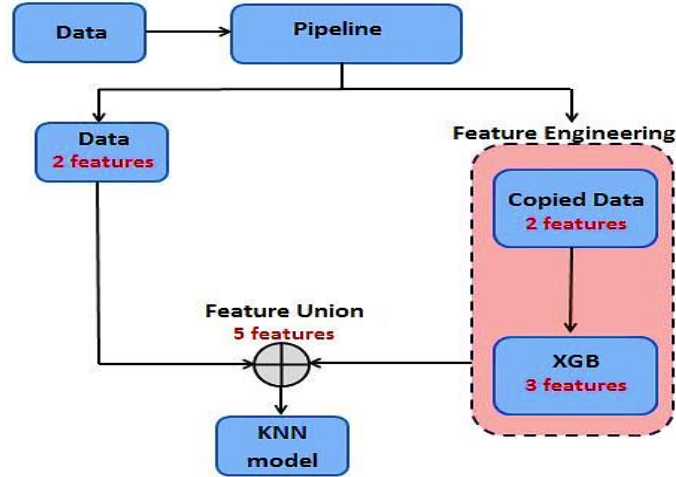


Fig.7: Resulted pipeline of the TPOT method.

2.3.5 Quantum neural network (QNN)

Despite the considerable advancements in quantum computing technologies and the exciting and fruitful race between giant tech companies, quantum computers are still noisy and cannot operate in room temperatures. That is why we are living in the noisy intermediate-scale quantum computers (NISQ) era [72]. ML helps us to take full advantage of these devices despite their erroneous behaviour. Using a hybrid quantum-classical computational model [73–75] paves the way for using the classical part to do the repeated procedures that require memory and error-correcting subroutines whereas the quantum part performs the complex intractable classical operations.

Different software libraries provide this framework of computation. PennyLane [74] is an example of these libraries. It provides the concept of a quantum node (Qnode) where you can perform an operation by providing the inputs to the parameterised gates and then measure the desired observable. In this manner, the Qnode is not interrupted until we perform the measurement. This concept of hybrid computation makes it easier to realise a fully quantum neural network where the backpropagation step on the classical part and the feedforward step on the quantum computer can be calculated. PennyLane also provides a means to calculate the gradients of the quantum gates without the help of any classical interference.

Relating the aforementioned idea to the typical ML pipeline, we need to determine the way of feeding the classical data into the quantum device and to choose an appropriate model for the task. There are two main techniques in quantum information science [76] to process the data; the Qubit model and the Continuous variable model [77–81]. Since our data are continuous, the CV model is chosen.

In the CV model, the information can be represented by the phase-space formalism [82,83], instead of the wavefunction formalism [84]. The former method is used as it's more convenient for our case. Generally, in this context, the data is encoded in terms of the \hat{x} and \hat{p} quadratures which satisfy the canonical relations by setting $\hbar = 2$:

$$[\hat{x}, \hat{p}] = 2i, \quad (11)$$

$$[\hat{a}, \hat{a}^\dagger] = I \quad (12).$$

These operators can be written in terms of each other as follows:

$$\hat{x} = (\hat{a} + \hat{a}^\dagger), \quad (13)$$

$$\hat{p} = i(\hat{a}^\dagger - \hat{a}), \quad (14)$$

where \hat{a} and \hat{a}^\dagger are the annihilation and the creation operators, respectively.

The basic state that can be converted into any desired state is the Vacuum state $|0\rangle$. The CV model has a set of gates that can be used to perform any mathematical operation or prepare any state. Moreover, due to its nature of processing the information, nonlinear gates are naturally present and are used to express its universality [85–87]. These gates are called Displacement, Squeezing, Rotation, and Beam Splitters, and the nonlinear gates are the Kerr and the Cubic Phase gates [77,78,83,88–90]. The nonlinear gates help with constructing higher-order Hamiltonians which are an incredible feat over the Qubit model, and one doesn't not require more than a single variable nonlinear gate for this construction.

The architecture of the QNN is adapted from ref.[86]. As depicted in Fig.8, we are only using one Qumode with a repeated block of gates. Each block represents a layer in terms of classical neural networks. The classical data is embedded in the quantum device by preparing a Displaced Squeezed state $|\alpha, z\rangle$ where $\alpha, z \in \mathbb{C}$ [91,92]. It is created by applying a Squeezing gate then followed by a Displacement gate.

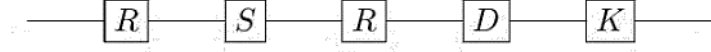


Fig.8: The configuration of the quantum circuit used for modelling.

Embedding classical data into quantum states is an active area of research [93–96]. Since we are only interested in measuring the \hat{x} quadrature and we’re embedding a classical neural network within a quantum framework; only the amplitudes of α and z are being used to encode the classical data of the I - V curve. The voltage values are scaled between [-1.1, 1] to be embedded by the displacement gate. The illumination values are scaled between [0, 0.8] to be used as the squeezing magnitudes.

This scheme of data encoding is depicted in Fig.9 (a,b) where the Wigner function has been plotted for a Vacuum state, the Displaced Squeezed state for the values $|0.6, 0.5\rangle$ and the final state of the quantum state after applying the learned parametrised circuit as shown in Fig.9.c. In terms of the quadratures, this would resemble a translation in the $\hat{x} \rightarrow S \hat{x} + d$ where S is the Squeezing gate, and its effect is simply narrowing the \hat{x} quadrature by e^{-r} and r is the $\Re(z)$, whereas d is the $\Re(\alpha)$ and it translates the \hat{x} from the origin by its magnitude. On the other hand, the \hat{p} quadrature is only affected by the S gate as it is stretching it by e^r .

According to [97], this mapping is critical to machine learning since it can be used as a kernel for feature mapping as the distance between two Displaced Squeezed states is calculated explicitly as follows [98]:

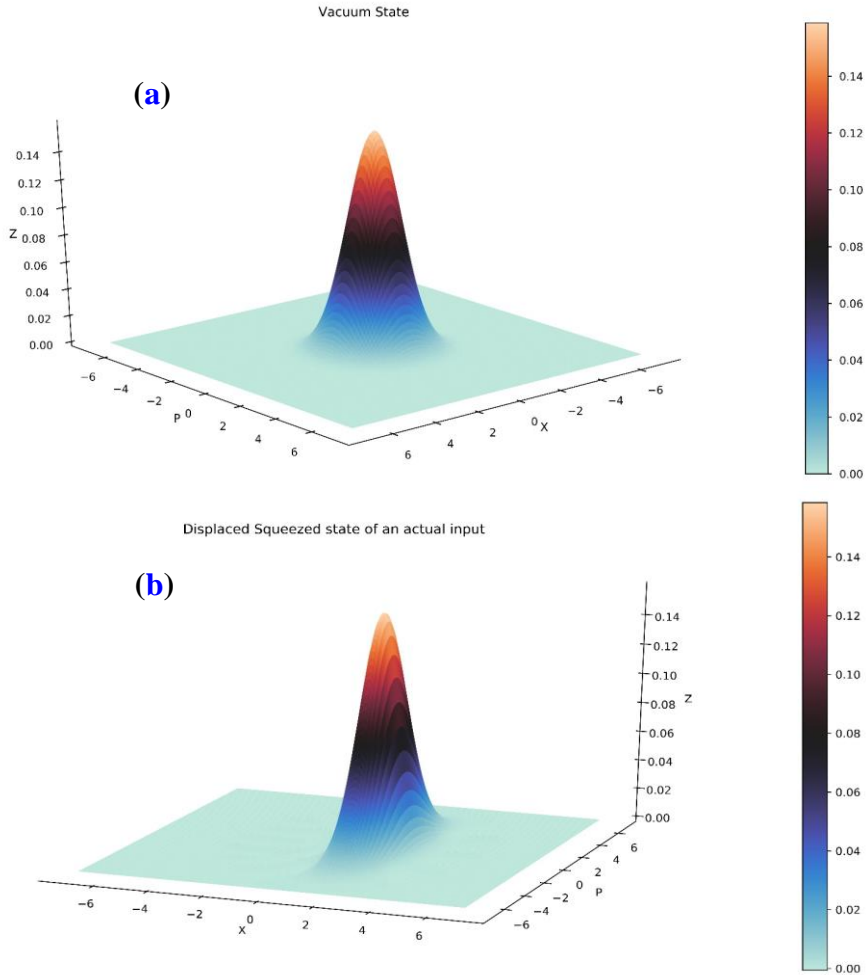
$$d(\langle \alpha_1, z_1 | \alpha_2, z_2 \rangle) = \sqrt{2(1 - |\langle \alpha_1, z_1 | \alpha_2, z_2 \rangle|^2)}, \quad (15)$$

where

$$\begin{aligned} \langle \alpha_1, z_1 | \alpha_2, z_2 \rangle &= \left(\frac{(1 - |z_2|^2)(1 - |z_1|^2)}{(1 - z_2 z_1^*)^2} \right)^{1/4} \\ &\times \exp \left\{ - \left[2(1 - z_2 z_1^*) \right]^{-1} \left((\alpha_2 + z_2 \alpha_2^*)(\alpha_2^* + z_1^* \alpha_2) \right. \right. \\ &\quad \left. \left. - 2(\alpha_2 + z_2 \alpha_2^*)(\alpha_1^* + z_1^* \alpha_1) + (\alpha_1 + z_2 \alpha_1^*)(\alpha_1^* + z_1^* \alpha_1) \right) \right\}, \end{aligned} \quad (16)$$

When the illumination is zero, then the prepared state is simply a Coherent state or a radial basis function kernel. This mapping procedure serves the regression problem we are trying to solve as we are only using a single Qumode to follow the architecture of [86].

Pennylane offers the means to evaluate the quantum gradients [74,99] of any quantum circuit. Following the same footsteps of classical NNs, this leaves us with determining the number of layers, the learning rate, the size of each batch and weight initialisation. So, the parametrised circuit consists of 7 layers; each layer consists of 5 parameters, i.e. it only has 35 parameters to be optimised by Adam optimiser. The batch size is 19, and we tried different settings for the learning rate starting from 0.001 till 0.01 . The weight initialisation was drawn from a random sample distribution with a standard deviation ranging from $[10^{-4}, 10^{-2}]$. The cut-off range was set to 14.



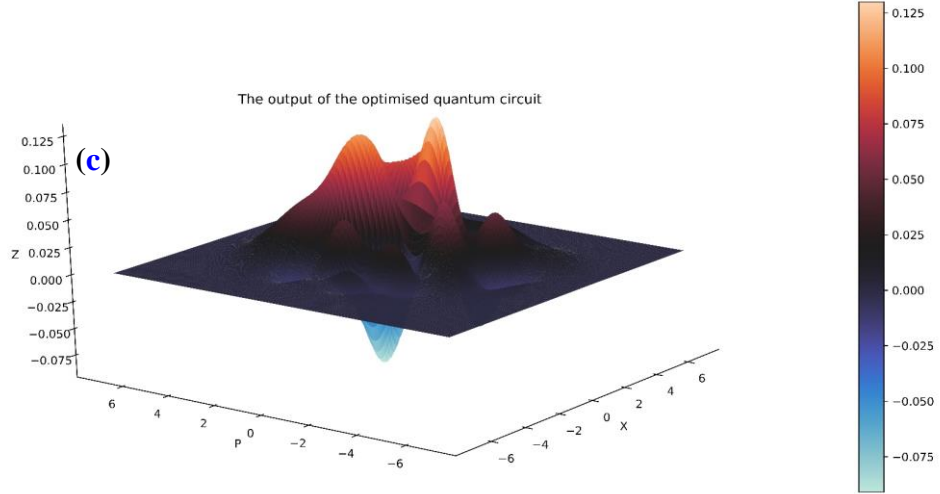


Fig.9: Wigner function of (a) vacuum state, (b) displaced-squeezed state and (c) quantum state.

3 Results and Discussion

3.1 Optical Characteristics of NTCDA Thin Film

For inspecting the most suitable spectral range of detection, the optical absorbance of NTCDA thin film is measured in the range 190-2500 nm. The absorption profile shown in Fig.10.a confirms the high UV absorption of NTCDA extended to the visible range with very low IR absorption. As observed from the inset of Fig.10.a, the intensity of the UV absorption peaks is more significant than that of the visible region which suggests a good selectivity to detect even a weak UV signal in a robust visible light background. The featured absorption peaks exhibited in the NTCDA absorption spectra implies the massive generation of photoexcited charge carriers in the NTCDA thin film. This leads to a high photocurrent and a high photoresponse photodetector. The optical band gap energy is estimated using absorption spectrum fitting (ASF) procedures [100,101]. The value of indirect energy gap can be estimated by extrapolating the linear portion of the plot of $(\text{Abs.} \lambda^{-1})^{1/2}$ versus λ^{-1} to $[(\text{Abs.} \lambda^{-1})^{1/2} = 0]$ as depicted in Fig.9.b which is corresponding to $1/\lambda_g$, where λ_g is the wavelength related to energy gap. The optical band energy can be estimated by $[E_g = hc/\lambda_g]$. The estimated values for the onset energy gap and the optical energy gap are about 2.84, and 3.75 eV, respectively.

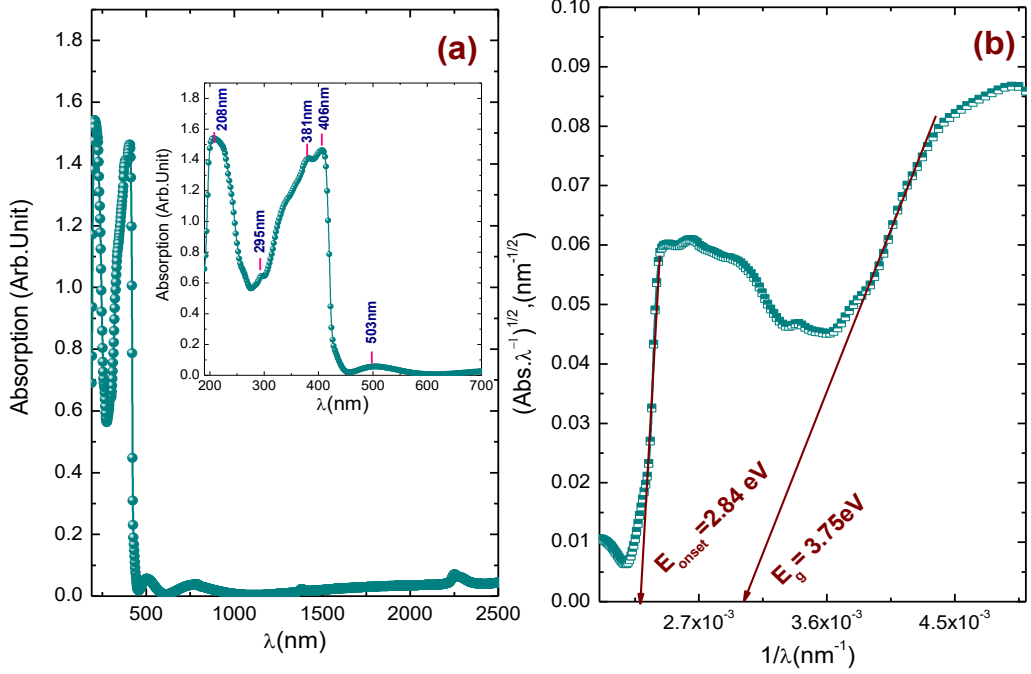


Fig.10: (a) Absorbance profile of NTCDA thin film, while the inset shows zoom-in on UV-visible absorbance and (b) estimating the onset and indirect energy gap of NTCDA thin film using ASF method.

3.2 Electrical Characteristics of Au/NTCDA/p-Si/Al Photodiode

Fig.11 depicts the semi-logarithmic current-voltage relation of Au/NTCDA/p-Si/ Al photodiode under the dark and illumination conditions at room temperature. A distinct rectification behaviour is obtained with ~ 3 and ~ 4 for dark and 80 mW/cm^2 irradiance at $\pm 3.5 \text{ V}$, respectively. A monotonic increase in the produced photocurrent is accompanied to the increase of light intensity. This increase emphasises the formation of neutral *Frenkel* excitons which dissociate generating free electrons and holes which are swept under the influence of the biasing voltage [30,102].

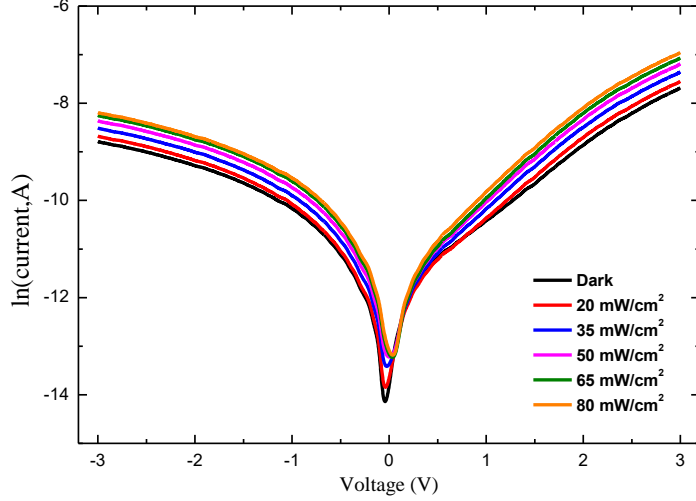


Fig.11: Semi-logarithmic plot of I - V characteristics of NTCDA/p-Si photodiode under different illumination intensities.

The thermionic emission theory was employed to fit the linear region of the forward-biased I - V curve at low voltages ($V_F < 0.15$ V) using the following relations [30,103]:

$$I = I_0 \exp\left(\frac{q(V - IR_s)}{nk_B T}\right) \left[1 - \exp\left(\frac{-q(V - IR_s)}{k_B T}\right)\right], \quad (17)$$

where I is the diode current, I_0 is the reverse saturation current, n is the ideality factor, q is the electron charge, k_B is Boltzmann constant, T is the temperature, R_s is the series resistance, and V is the applied voltage. The reverse saturation current and the barrier height at zero voltage, Φ_{Bo} , are interrelated by the following equation [30,103]:

$$\phi_{Bo} = \frac{k_B T}{q} \ln\left(\frac{AA^* T^2}{I_0}\right), \quad (18)$$

where A is the active area of the device, A^* is the effective Richardson constant.

The ideality factor, n , was estimated from the slope of the linear region of the I - V curve in forward biasing with neglecting the series resistance in the low voltage region $V_F < 0.18$ V using the following relation [30]:

$$n = \frac{q}{k_B T} \left[\frac{dV}{d(\ln I)} \right], \quad (19)$$

Upon illumination, the estimated values of the ideality factor were decreased from 4.98 (in the dark) to 3.78 (under 80 mW/cm² irradiance). The high values of ideality factor over-unity may be attributed to many factors such as tunnelling process [104], the image-forces effect

[105], series resistance [106], inhomogeneity of barrier height and the existence of interface states [107,108]. Herein, the series resistance and the interfacial layer existence have the primary responsibility of the high value of ideality factor. Moreover, a slight increase in the values of zero-bias barrier height from 0.7 eV (in the dark) to 0.72 eV (under 80 mW/cm² irradiance) which may be attributed to the passivation of Si surface by NTCDA [103].

Inherently, the series resistance has a crucial impact on the performance of any electronic device, where these types of devices always exhibit a high series resistance. In this essence, many models were developed to estimate the values of series resistance, but each model has its limitations [109]. Subsequently, the series resistance of the fabricated device was estimated using a modified *Nord's* model, which is applicable to the whole voltage range [108–111]. A significant decrement in the series resistance from 2.96 kΩ to 0.10 kΩ upon increasing the illumination intensity from 0 mW/cm² to 80 mW/cm² is observed. This decrement may be explained as follows; under the influence of illumination, the photo-generated charge carriers would be trapped at either at p-Si/NTCDA interface or NTCDA/ electrode interface. Increasing the illumination intensity increases the density of photo-generated charge carriers and decreases the probability of trapping charges, decreasing the series resistance [108,112].

The estimated high values of ideality factor indicates that thermionic emission is no longer suitable for interpreting the transport mechanism, so to investigate the operating charge transport mechanisms in Au/NTCDA/p-Si/Al photodiode, the double logarithmic relation between current and voltage in forward biasing in dark and under 80 mW/cm² irradiance are plotted as shown in Fig.12.a. Two distinct regions with different slopes are obtained; region (I) of slope equals one and region (II) of slope equals 2.62. The dominant transport mechanism in the region (I) is the Ohmic transport mechanism [113], while in the region (II) the dominant transport mechanism is the space charge limited conduction (SCLC) that is dependent on trap level density and interface states [113,114].

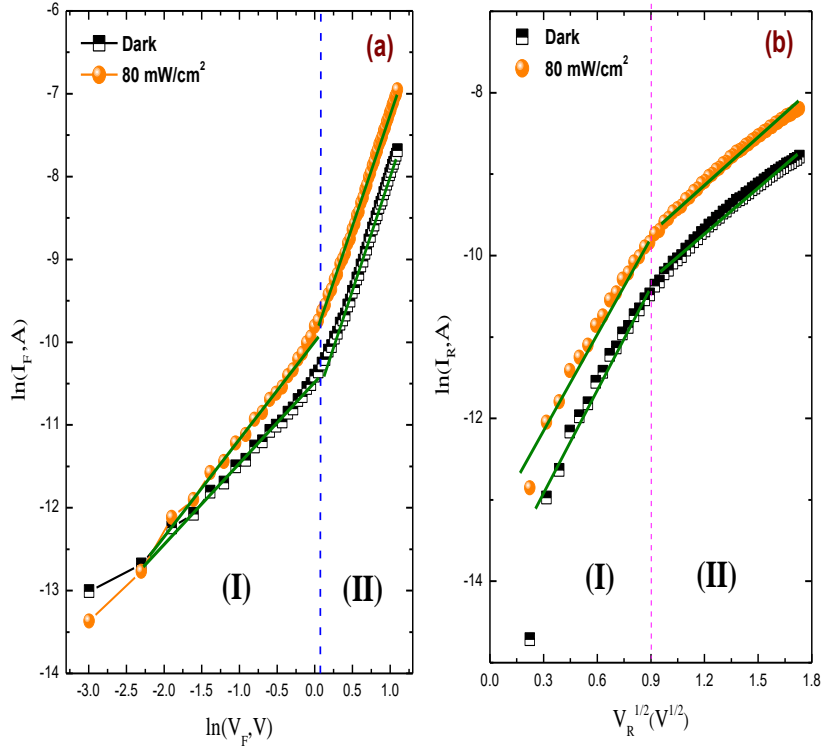


Fig.12: (a) $\ln(I_F)$ versus $\ln(V_F)$ and (b) $\ln(I_R)$ versus $V_R^{1/2}$ for NTCDA/p-Si photodiode in dark and under 80 mW/cm² illumination.

Furthermore, the transport conduction mechanism in reverse biasing of Au/NTCDA/p-Si/Al photodiode is investigated by plotting the relation between $V_R^{1/2} - \ln I_R$ in the dark and under 80 mW/cm² as shown in Fig.12.b. Two linear regions of different slopes were obtained which may be attributed to either *Schottky* or *Poole-Frenkel* mechanism.

According to *Schottky* conduction mechanism, the reverse current can be represented as following [114]:

$$I_{Sc,R} = A A^* T^2 \exp\left(\frac{-\phi_B}{k_B T}\right) \exp\left(\frac{\beta_{Sc} E^{1/2}}{k_B T}\right), \quad (20)$$

where E is the applied electric field, and β_{Sc} is the *Schottky* field lowering coefficient. Based on the *Poole-Frenkel* emission mechanism, the reverse current can be represented as following [114]:

$$I_{PF,R} = I_s A \exp\left(\frac{\beta_{PF} E^{1/2}}{k_B T}\right), \quad (21)$$

where β_{PF} is *Poole-Frenkel* coefficient. The value of β is given by [114]:

$$\beta = \left(\frac{q^3}{b \pi \epsilon \epsilon_0} \right)^{1/2}, \quad (22)$$

where b is a constant equals 1 for *Poole-Frenkel* mechanism and equals 4 for *Schottky* mechanism [114], ϵ is the dielectric constant of the material ($\epsilon = 2.89$ [115]), ϵ_0 is the permittivity of free space ($8.85 \times 10^{-12} \text{ F/m}^2$) and q is electron's charge. The calculated values of β were about $4.46 \times 10^{-5} \text{ eVm}^{1/2} \text{V}^{1/2}$ for *Poole-Frenkel* mechanism and $2.23 \times 10^{-5} \text{ eVm}^{1/2} \text{V}^{1/2}$ for *Schottky* mechanism. The experimental values of β estimated from the slope of the straight lines in the region (I) and region (II) were about $4.89 \times 10^{-5} \text{ eVm}^{1/2} \text{V}^{1/2}$ and $2.05 \times 10^{-5} \text{ eVm}^{1/2} \text{V}^{1/2}$, respectively. Hence, the transport mechanism in the low voltage region (I) is interpreted as a *Poole-Frenkel* mechanism, while in the high voltage region (II) is interpreted as a *Schottky* emission mechanism.

3.3 Optoelectronic Characteristics of Au/NTCDA/p-Si/Al Photodiode

An explicit investigation of photosensitivity of the fabricated photodiode was performed by studying the dependence of photocurrent density, J_{Ph} , on illumination intensity at different biasing voltages as shown in Fig.13.a. The fabricated device exhibits a linear performance with the irradiance up to 65 mW/cm^2 , but exceeding this limit makes the photodiode saturates. The linearity of photocurrent density and irradiance relation is more obvious in the high biasing voltages than lower voltages. Fig.13.b shows the double logarithmic relation between the photocurrent, I_{Ph} , and incident power, P , where the estimated slopes (~ 1.4) conclude that this architecture can be utilised in optoelectronic applications to detect low-intensity signals.

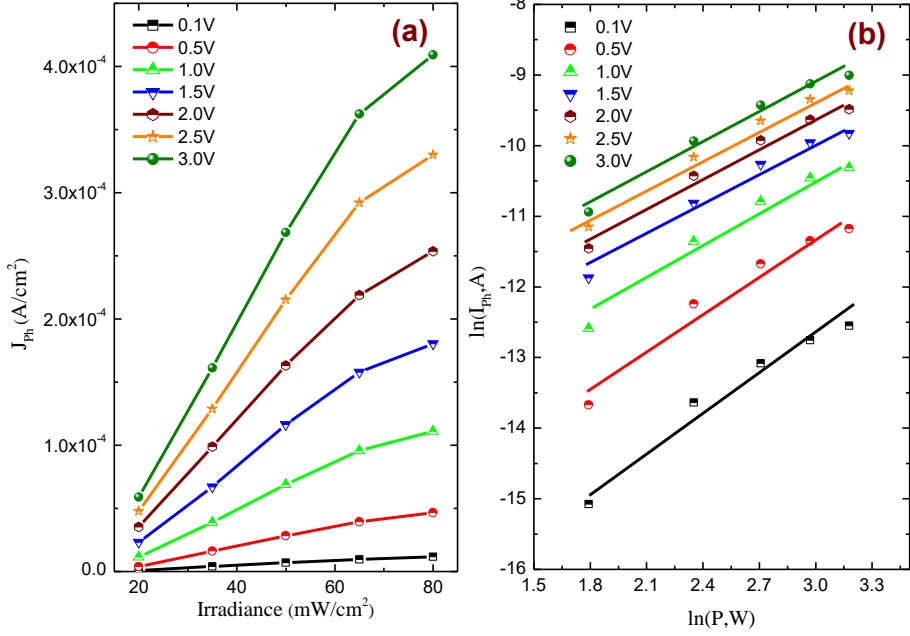


Fig.13: (a) The irradiance-photocurrent density relation and (b) $\ln P$ versus $\ln I_{ph}$ for NTCDA/p-Si photodiode at different biasing voltages.

The quantitative evaluation of the optoelectronic performance of the existing architecture necessitates an accurate estimation of several figures of merit. s

$$R = \frac{J_{ph}}{P}, \quad (23)$$

$$D^* = \frac{R}{\sqrt{2qJ_{dark}}} = D \times \sqrt{A}, \quad (24)$$

$$EQE = \frac{hc}{\lambda q} \times R \times 100, \quad (25)$$

$$I_N = NEP \cdot R = \frac{R \sqrt{A}}{D^*}, \quad (26)$$

where NEP is the noise equivalent power. Fig.14 shows the voltage dependence of responsivity, specific detectivity, external quantum efficiency and noise current at different illumination intensities. An apparent increase of responsivity, specific detectivity, and external quantum efficiency with increasing the illumination intensity up to 65 mW/cm², which means that this architecture operates for detecting a light signal of illumination lower than 65 mW/cm². The decrease of photoresponsivity of the fabricated device at intensity 80 mW/cm² may be attributed to the decrease of sufficient photo-induced trap states density at the interface [117]. The calculated specific detectivity which determines the resolution limit that the detector can

distinguish from the noise [118] is in the range of 10^9 Jones as shown in Fig.14.b which proves the sensitivity of the fabricated device [117]. From Fig.14.c, the *EQE* of the fabricated photodiode records the highest value at 65 mW/cm^2 illumination and -3.5 V biasing voltage. Inherently, there are three contributions to noise current in photodetector should be considered; thermal noise or Johnson noise current (I_J), shot noise current (I_{Sh}) and flicker noise current (I_{Fl}) [119]. The estimated values of noise current were about 0.4 pA and 7 pA at 0 V and -3 V , respectively. The absence of effective influence of the light intensity on the noise current, as shown in Fig.14.d proves that the shot noise from dark current density is the main responsible for noises in the photodiode [119,120]. Table.2 shows a comparison study between the estimated parameters of the present device and previous work.

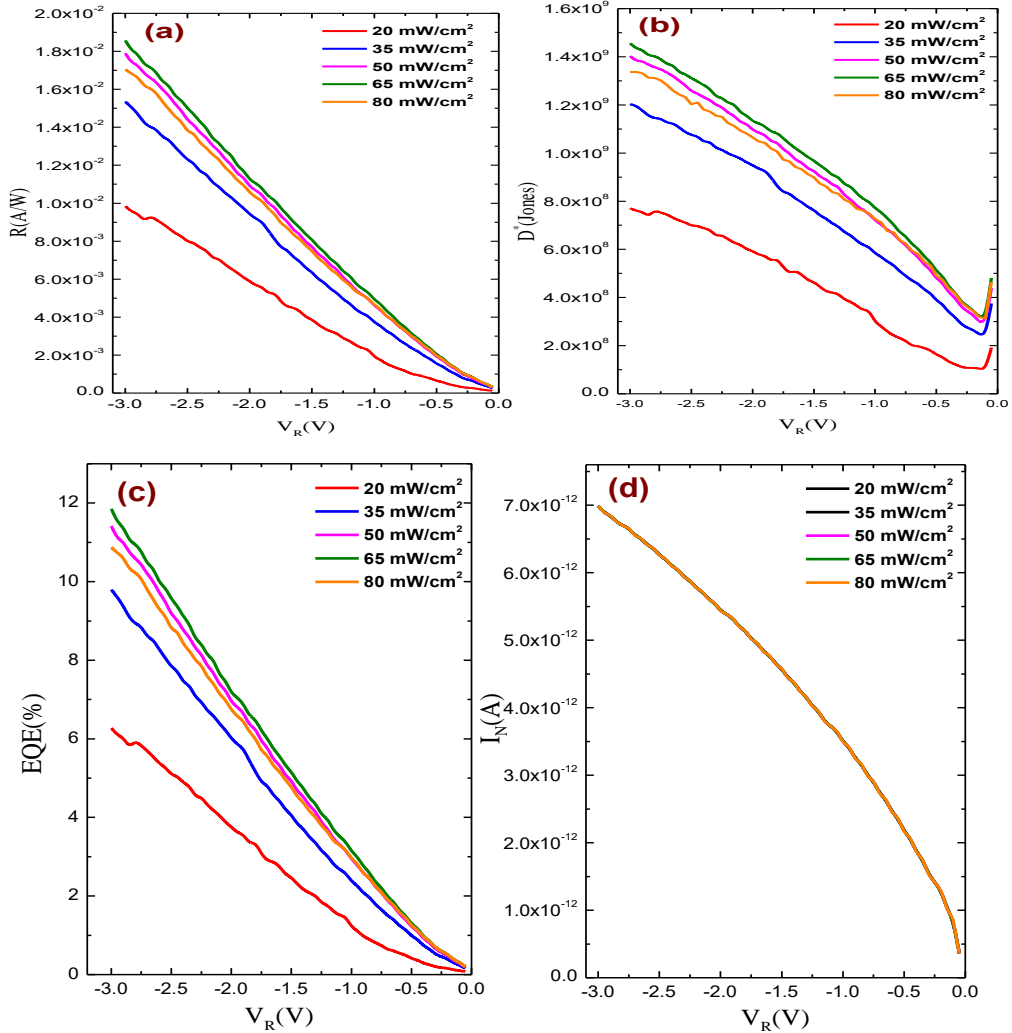


Fig.14: The voltage dependence of (a) responsivity, (b) specific detectivity, (c) external quantum efficiency and (d) noise current of the fabricated device at different illumination intensities.

Table 2: The performance parameters of some UV and visible Si-based photodiodes.

photodiode structure	Detection band	Responsivity (mA/W)	Specific detectivity (Jones)	EQE (%)	Rise time	Fall time	Ref
NTCDA/p-Si at 65 mW/cm ²	UV	19 (at= -3 V)	1.5×10^9 (at= -3 V)	11.85	433 ms	495 ms	Present work
Cu(acac) ₂ /n-Si at 80 mW/cm ²	UV and Visible	4.7 (at= -3.5 V)	2.7×10^9 (at= -3.5 V)	5.53	339 ms	1046 ms	[108]
TiOPc/p-Si at 180 mW/cm ²	IR	1.63×10^{-2} (at= -2V)	1.22×10^7 (at= -2 V)	0.25	23 μ s	34 μ s	[121]
PTCDI/p-Si at 200mW/cm ²	IR	0.2 (at= 0 V)	7×10^7 (at= 0 V)	—	300 ns	300 ns	[122]
P-quaterphenyl /p-Si	UV and Visible	9 (at= -1 V)	1.14×10^8 (at= -1 V)	—	25 μ s	—	[123]
Au/ α -6T/n-Si at 2560 mW/cm ²	UV and Visible	0.2 (at -2.5 V)	1.2×10^8 (at -2.5 V)	0.3	410 ms	400 ms	[124]

The photoresponse speed of any optical device plays a crucial role in evaluating its optoelectronic performance, where almost all the optical devices require picking up a light signal with a certain bandwidth with fast response. The photoresponse speed which measures the quickness of extracting the photo-generated charge carriers to the external electrical circuit is dependent on many factors such as active layer thickness, the choice of interfacial layer material and applied biasing voltage [125]. Fig.15 shows the transient photocurrent response of the fabricated photodiode under the influence of the square UV signal of 0.1 Hz frequency at different illumination intensities and 1V biasing voltage. The illustrated time-tracked photocurrent is evidence of the strong and fast photoresponse of the existing architecture with good repetition and stability. Furthermore, it is observed that Au/NTCDA/p-Si/Al photodiode has a residual photocurrent in the OFF state which increases slightly with increasing the illumination intensity. This may be explained in terms of enhancement of NTCDA photoconductivity due to photo-thermal energy emitted of the incident light [108]. Fig.16 (a-d) reveals the fall time

and rise time assessment for the fabricated photodiode under 20, 35, 65 and 80 mW/cm^2 illuminating intensity. A clear decrease of fall and rise times is noticed upon increasing the illumination intensity. Moreover, the ON/OFF ratio for different irradiance values at different reverse biasing voltages is estimated as shown in Fig.16.e. For high irradiance values ($> 20 \text{ mW/cm}^2$), the most appropriate biasing voltage is 1V to get higher ON/OFF ratio, while at 20 mW/cm^2 increasing the applied voltage increases the ON/OFF ratio.

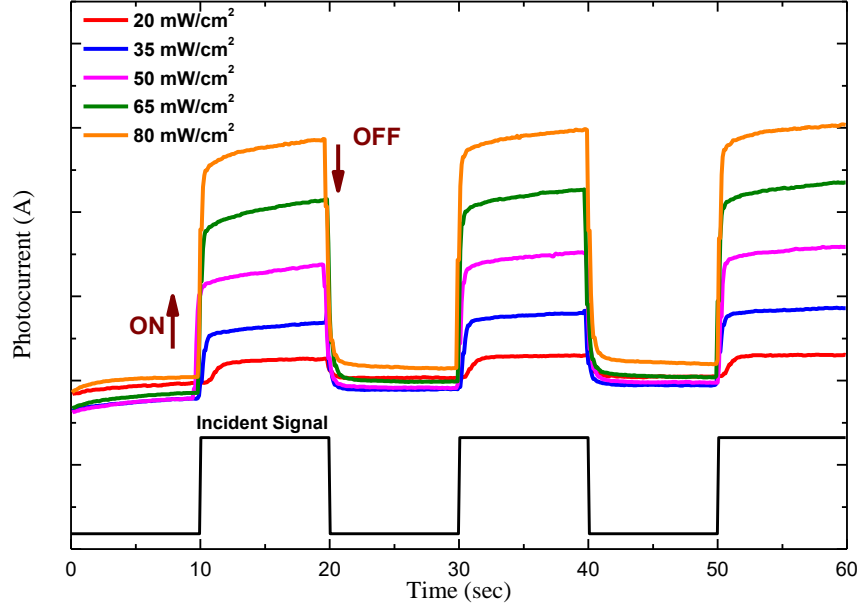
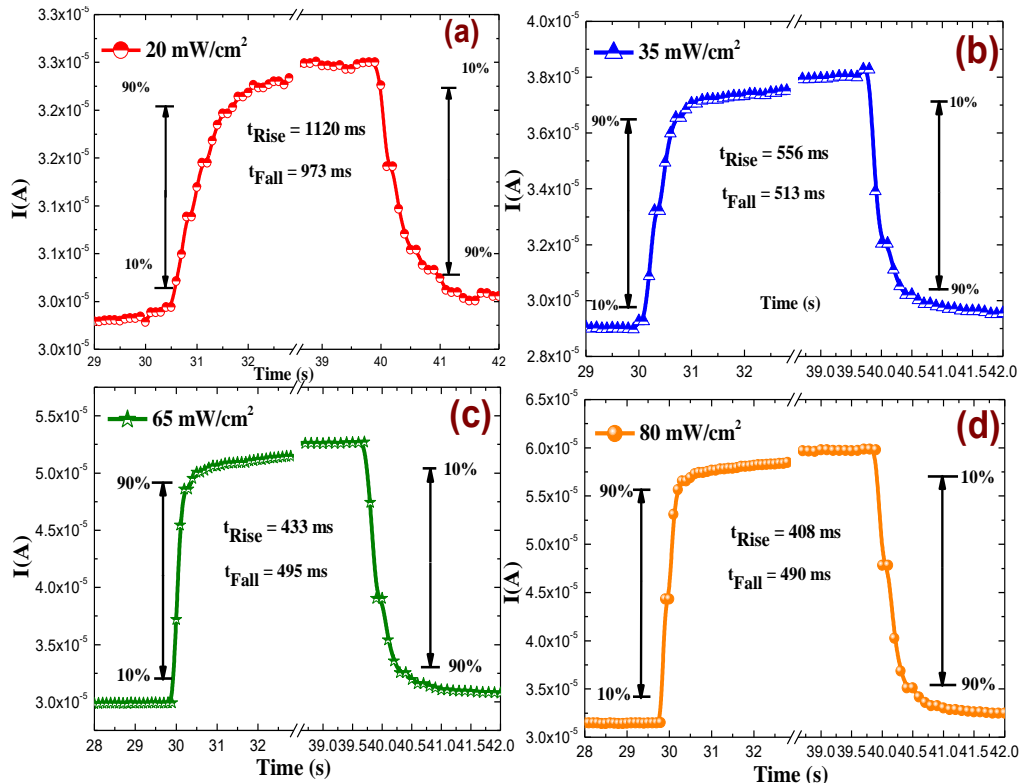


Fig.15: Repeatable ON/OFF switching behaviour of the fabricated photodiode under different illumination intensities at 1 V.



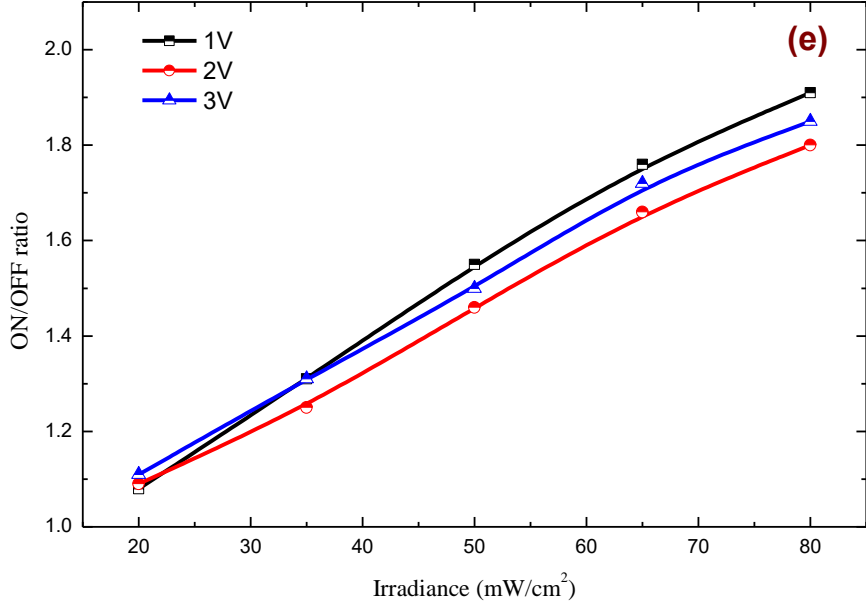


Fig.16: The analysis of rise and fall time of Au/NTCDA/p-Si/Al photodiode under (a) 20 mW/cm², (b) 35 mW/cm², (c) 65mW/cm², (d) 80 mW/cm² irradiance and (e) ON/OFF ratio – irradiance relation at different biasing voltages.

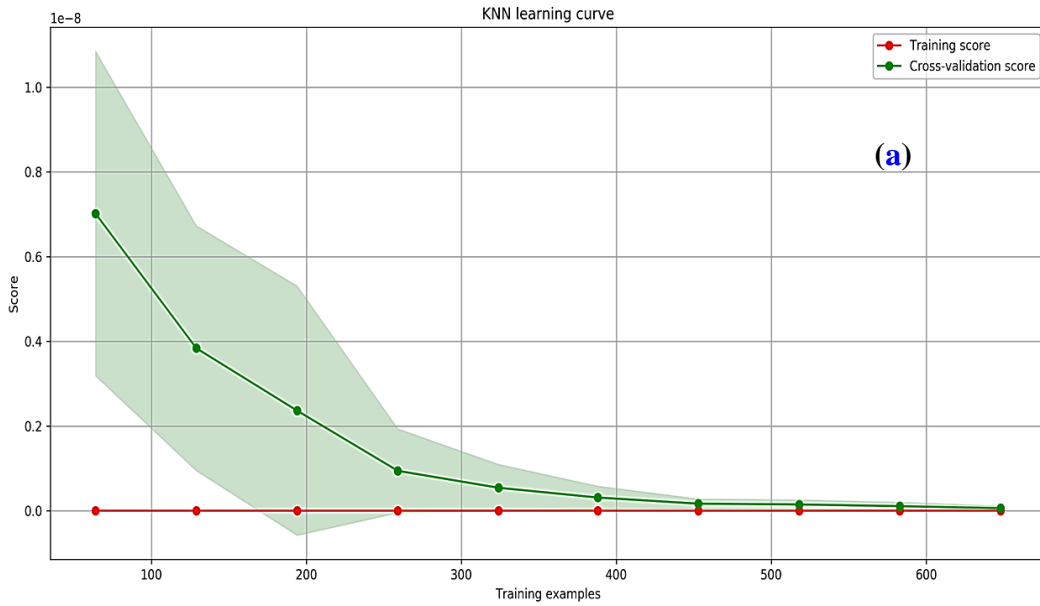
3.4 Modelling the Optoelectronic Characteristics of Au/NTCDA/p-Si/Al Photodiode

To make our results reproducible and consistent, we paid careful attention to the randomness that may occur while splitting the data into the training and testing sets or even the stochastic nature of the NNs. Moreover, we trained all of the algorithms on the same partitioning so that we can compare the performance of each one with the others. We set 15% of the data to be the testing set and the other 85% to be the training data. The traditional machine learning algorithms were adopted from Scikit-Learn and TPOT [67,126]. For the ANN part, Keras and TensorFlow [65,127] were used. Pennylane and StrawberryFields [74,128] were used to model the QNN and to study its characteristics. The final results of the four models are presented in table.3.

Fig.17.a depicts the learning curve of the first model (KNN). This learning curve proves that the model fits the data correctly and avoids overfitting. Its parameters are $K = 4$, $P = 4$. The metric function is the Minkowski, and the searching algorithm is the Brute Force. From table.3, it is obvious that the KNN comes at the second place after the ANN model. Fig.17.b reveals the loss of both of the training and the validation of the ANN. Due to the nature of the Adam optimiser; the loss keeps oscillating but with a minimal variance after **10000** epochs. With a batch size of **19** and a learning rate of 10^{-3} , the ANN achieved the lowest error rate amongst them.

Despite being fed with raw data directly, the automated approach managed to achieve a reasonable error rate. Nevertheless, we had to configure its dictionary of parameters to eliminate specific methods of feature engineering such as Radial Basis Function Sampler [129] and Polynomial Features [34]; because they produced overfitted pipelines despite the cross-validation mechanism, it follows. In Fig 17.c, the learning curve of the TPOT shows very similar behaviour to the KNN model. The first three approaches (KNN, ANN, TPOT) can predict intermediate values i.e. they can extrapolate values that they have never been trained on. Moreover, they can predict an accurate estimate of extreme values below **0.05** towards zero and above **3.5** volts.

Finally, in terms of accuracy, the QNN achieved the highest error rate with a relatively small number of epochs around **400**. However, in terms of complexity, by using only one Qumode with a relatively shallow circuit, we managed with reasonable accuracy to model the behaviour of the diode. In Fig 17.d, both of the training and the testing losses are depicted. The QNN shows a very promising convergence rate in comparison with the classical NN. Despite using the Adam optimiser for training the QNN, the learning curve is smoother than the curve of the classical neural network.



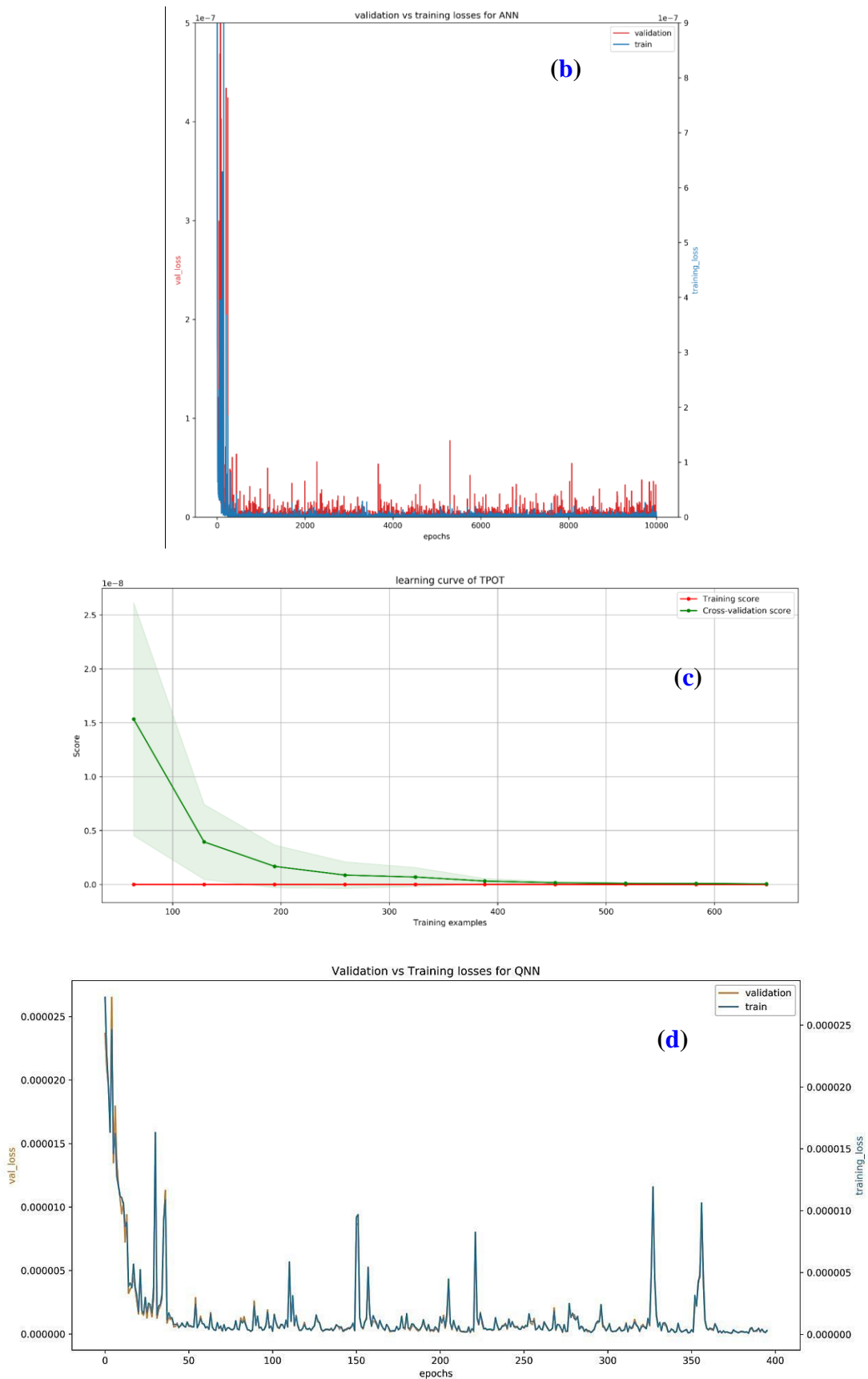
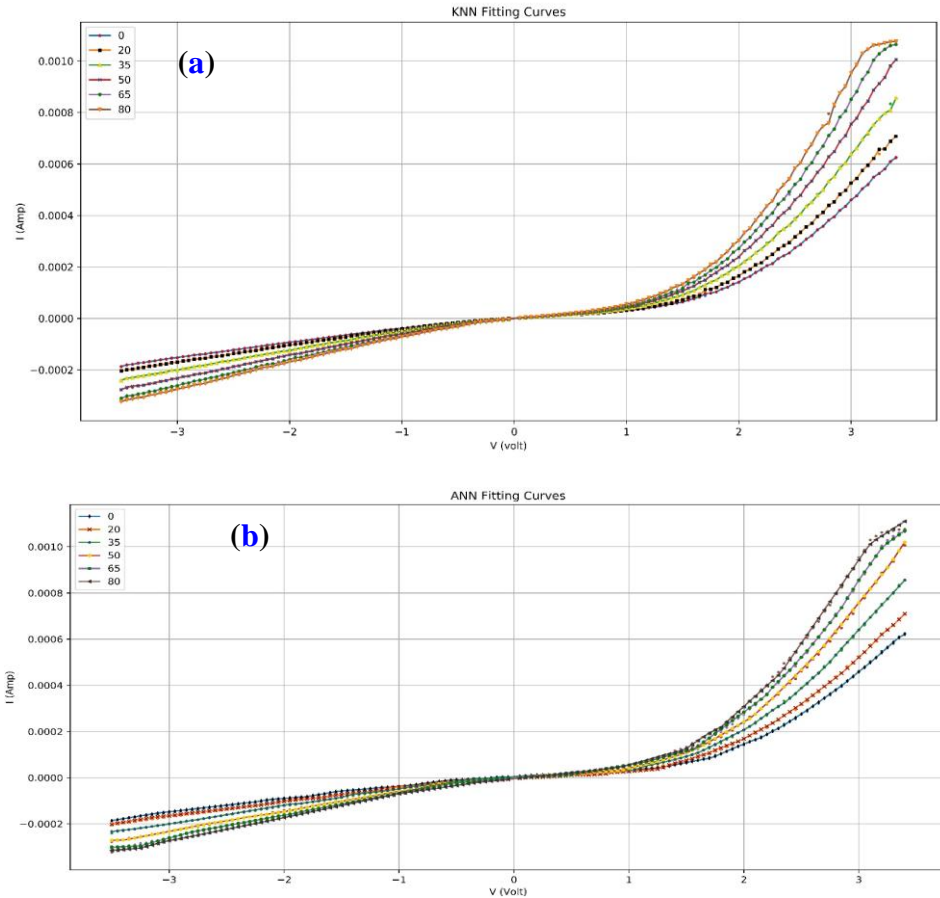


Fig.17: The learning curves of (a) KNN, (b) ANN, (c) TPOT and (d) QNN models.

There are important observations regarding the process of training the QNN. Due to the unitary nature of the quantum gates and also the bounded Hilbert space, we had to rescale the target values by 1000 to accommodate the homodyne measurement of the x quadrature. To keep the value of the trace near to unity, weight initialisation was drawn from a normal distribution with a standard deviation that ranges between $[10^{-4}, 10^{-2}]$ and the chosen learning rate has not exceeded 0.01 throughout the experimentation. Increasing the capacity of the QNN by using the phase variables of the squeezing and the displacement gates does help with converging faster.

It has been observed due to the high squeezing amplitudes that a cut-off range between 14 and 18 is good enough for simulating the system without critical loss of information. The Cubic Phase gate does require a high cut-off dimension starting from 18 and above. However, it accelerates the convergence process noticeably.

Fig 18(a-d) shows the performance of the utilised models to solve this regression problem. The scattered points in these figures represent the measured data. The drawn lines are the simulated data from the models.



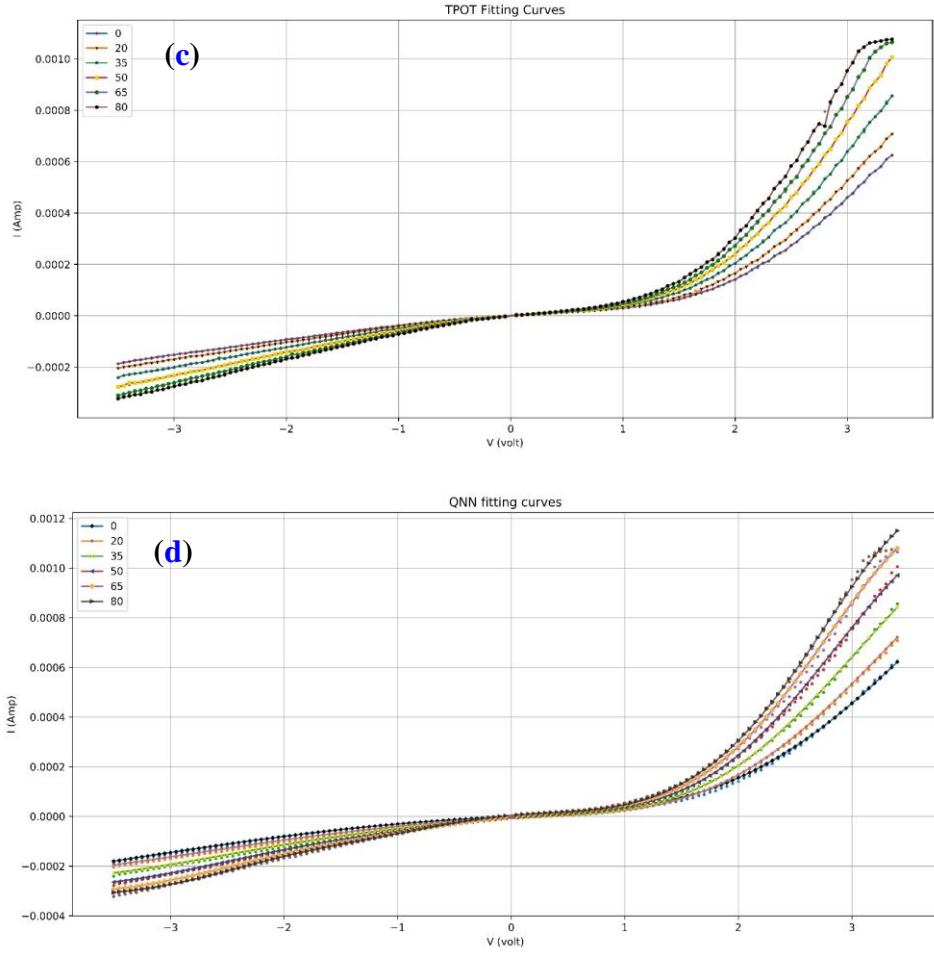


Fig.18: The fitted experimental data of I - V characteristic curve of NTCDA/p-Si using (a) KNN, (b) ANN, (c) TPOT and (d) QNN models.

Table.3: the obtained values of the mean squared error resulted from the four models.

Method	Train	Test	Validation
KNN	0	2.67×10^{-11}	6.07×10^{-11}
TPOT	0	3.58×10^{-11}	5.38×10^{-11}
ANN	2.25×10^{-11}	1.6812×10^{-11}	-
QNN	8.88×10^{-11}	5.77×10^{-11}	-

4 Conclusion

Organic/inorganic heterojunction based on NTCDA/p-Si was successfully fabricated for UV light detection manner. According to the obtained values of spectral responsivity, linear-dynamic range, specific detectivity, signal to noise ratio, and response time for the fabricated photodiode under the influence of UV light of intensity 20-80 mW/cm², the current device is

suggested for many optoelectronic applications. These obtained results ensure that the optimum light intensity where this detector works efficiently is 50 mW/cm².

Regarding the modelling section of this research, adopting a regression analysis approach resulted in three accurate classical algorithms that can be used to model and predict the behaviour of the fabricated device. These models can both extrapolate and interpolate unknown current values under different illuminations and voltage settings.

Furthermore, they can predict extreme values near zero voltage with a minimal error rate. This can help other researchers conduct their studies without going through the costly manufacturing process. Using the fourth model, i.e. the QNN, we managed experimentally to show the superiority of the Qumode as it can encode floating-point data easily. In addition to that, a single Qumode with only 35 parameters has the capability of reproducing what a classical fully connected NN can do with thousands of parameters. This is a powerful indicator of the universality of the CV model.

The only drawback that we faced with the QNN approach is that we needed to scale the target values. As shown by the inspection section, the current values are minimal. However, the outputs from the quantum gates are around unity. Hence, in our future work, we aim to study the effect of encoding the data on the final result and also the behaviour of the optimisation mechanism on the quantum state.

Acknowledgements

The authors would like to express their most profound appreciation to Prof. Zoltán Zimborás from Wigner Research Centre for Physics, Hungarian Academy of Sciences and Dr. Josh Izaac from the University of Western Australia for their helpful discussions and keynotes.

Funding

This research did not receive any specific grant from funding agencies in the public, commercial, or not-for-profit sectors.

References

- [1] J. Han, J. Wang, Photodetectors based on two-dimensional materials and organic thin-film heterojunctions, *Chinese Phys. B.* 28 (2019) 017103. doi:10.1088/1674-1056/28/1/017103.
- [2] M. Häming, A. Schöll, E. Umbach, F. Reinert, Adsorbate-substrate charge transfer and electron-hole correlation at adsorbate/metal interfaces, *Phys. Rev. B.* 85 (2012) 235132. doi:10.1103/PhysRevB.85.235132.
- [3] R. Tonner, P. Rosenow, P. Jakob, Molecular structure and vibrations of NTCDA monolayers on Ag(111) from density-functional theory and infrared absorption spectroscopy, *Phys. Chem. Chem. Phys.* 18 (2016) 6316–6328. doi:10.1039/C5CP06619K.

[4] H. Tachikawa, H. Kawabata, A density functional theory study on the degradation mechanism of thin film of organic semiconductor by water molecules, *Thin Solid Films.* 516 (2008) 3287–3293. doi:10.1016/j.tsf.2007.08.108.

[5] H. Tachikawa, H. Kawabata, Electronic states of alkali metal-NTCDA complexes: A DFT study, *Solid State Sciences.* 48 (2015) 141–146. doi:10.1016/j.solidstatesciences.2015.08.002.

[6] X. Han, F. Yi, T. Sun, J. Sun, Synthesis and electrochemical performance of Li and Ni 1,4,5,8-naphthalenetetracarboxylates as anodes for Li-ion batteries, *Electrochemistry Communications.* 25 (2012) 136–139. doi:10.1016/j.elecom.2012.09.014.

[7] L. Torsi, A. Dodabalapur, N. Cioffi, L. Sabbatini, P.G. Zambonin, NTCDA organic thin-film-transistor as humidity sensor: weaknesses and strengths, *Sensors and Actuators B: Chemical.* 77 (2001) 7–11. doi:[https://doi.org/10.1016/S0925-4005\(01\)00664-5](https://doi.org/10.1016/S0925-4005(01)00664-5).

[8] H.E. Katz, A.J. Lovinger, J. Johnson, C. Kloc, T. Siegrist, W. Li, Y.-Y. Lin, A. Dodabalapur, A soluble and air-stable organic semiconductor with high electron mobility, *Nature.* 404 (2000) 478–481. doi:10.1038/35006603.

[9] S.T. Pérez-Merchancano, G.E. Marques, L.E. Bolivar-Marinez, Optical transitions in new trends organic materials, *Microelectronics Journal.* 39 (2008) 576–578. doi:10.1016/j.mejo.2007.07.033.

[10] H. Abdel-Khalek, E. Shalaan, M.A.- El Salam, A.M. El-Sagheer, A.M. El-Mahalawy, Effect of thermal annealing on structural, linear and nonlinear optical properties of 1, 4, 5, 8-naphthalene tetracarboxylic dianhydride thin films, *Journal of Molecular Structure.* 1178 (2019) 408–419. doi:10.1016/j.molstruc.2018.10.058.

[11] S. Tanida, K. Noda, H. Kawabata, K. Matsushige, N-channel thin-film transistors based on 1,4,5,8-naphthalene tetracarboxylic dianhydride with ultrathin polymer gate buffer layer, *Thin Solid Films.* 518 (2009) 571–574. doi:10.1016/j.tsf.2009.07.019.

[12] W.T. Hammond, J.P. Mudrick, J. Xue, Balancing high gain and bandwidth in multilayer organic photodetectors with tailored carrier blocking layers, *Journal of Applied Physics.* 116 (2014) 214501. doi:10.1063/1.4902149.

[13] M. Hiramoto, A. Miki, M. Yoshida, M. Yokoyama, Photocurrent multiplication in organic single crystals, *Appl. Phys. Lett.* 81 (2002) 1500–1502. doi:10.1063/1.1501764.

[14] Y.-M. Koo, O.-K. Song, Spontaneous charge transfer from indium tin oxide to organic molecules for effective hole injection, *Appl. Phys. Lett.* 94 (2009) 153302. doi:10.1063/1.3119860.

[15] T. Katsume, M. Hiramoto, M. Yokoyama, Photocurrent multiplication in naphthalene tetracarboxylic anhydride film at room temperature, *Appl. Phys. Lett.* 69 (1996) 3722–3724. doi:10.1063/1.117201.

[16] S. Forrest, F. So, Organic optoelectronic devices and methods, n.d. <https://experts.umich.edu/details/patent/US-5315129-A>.

[17] K.-S. Kim, S.-C. Park, J.-G. Nam, M. Hiramoto, Organic photoelectric conversion film, and photoelectric conversion device and image sensor each having the organic photoelectric conversion film, US20090294761A1, 2009. <https://patents.google.com/patent/US20090294761A1/en> (accessed October 2, 2019).

[18] C. Falkenberg, C. Uhrich, B. Maennig, M. K. Riede, K. Leo, 1,4,5,8-Naphthalenetetracarboxylic dianhydride as transparent electron transport material in organic p-i-n solar cells, in: 2008. <https://doi.org/10.1117/12.782340>.

[19] B. Lassiter, G. Wei, S. Wang, J. Zimmerman, V. Diev, M. Thompson, S. Forrest, Organic photovoltaics incorporating electron conducting exciton blocking layers, *Applied Physics Letters.* 98 (2011) 243307. doi:10.1063/1.3598426.

[20] G. Liang, T. Cui, K. Varahramyan, Electrical characteristics of diodes fabricated with organic semiconductors, *Microelectronic Engineering.* 65 (2003) 279–284. doi:10.1016/S0167-9317(02)00901-2.

[21] M. Zhu, G. Liang, T. Cui, K. Varahramyan, Depletion-mode n-channel organic field-effect transistors based on NTCDA, *Solid-State Electronics.* 47 (2003) 1855–1858. doi:10.1016/S0038-1101(03)00141-2.

[22] L. Torsi, Novel applications of organic based thin film transistors, *Microelectronics Reliability.* 40 (2000) 779–782. doi:10.1016/S0026-2714(99)00284-X.

[23] L. Torsi, A. Dodabalapur, L. Sabbatini, P.G. Zambonin, Multi-parameter gas sensors based on organic thin-film-transistors, *Sensors and Actuators B: Chemical.* 67 (2000) 312–316. doi:10.1016/S0925-4005(00)00541-4.

[24] A.A.A. Darwish, T.A. Hanafy, A.A. Attia, D.M. Habashy, M.Y. El-Bakry, M.M. El-Nahass, Optoelectronic performance and artificial neural networks (ANNs) modeling of n-InSe/p-Si solar cell, *Superlattices and Microstructures.* 83 (2015) 299–309. doi:10.1016/j.spmi.2015.03.033.

[25] E. Karatepe, M. Boztepe, M. Colak, Neural network based solar cell model, *Energy Conversion and Management.* 47 (2006) 1159–1178. doi:10.1016/j.enconman.2005.07.007.

[26] X. Lin, Z. Si, W. Fu, J. Yang, S. Guo, Y. Cao, J. Zhang, X. Wang, P. Liu, K. Jiang, W. Zhao, Intelligent identification of two-dimensional nanostructures by machine-learning optical microscopy, *Nano Res.* 11 (2018) 6316–6324. doi:10.1007/s12274-018-2155-0.

[27] A.A. Attia, M.M. El-Nahass, M.Y. El-Bakry, D.M. Habashy, Neural networks modeling for refractive indices of semiconductors, *Optics Communications.* 287 (2013) 140–144. doi:10.1016/j.optcom.2012.09.016.

[28] B. Rouet-Leduc, Machine Learning for Materials Science, Thesis, University of Cambridge, 2017. <https://doi.org/10.17863/CAM.13918> (accessed October 2, 2019).

[29] Y. Liu, T. Zhao, W. Ju, S. Shi, Materials discovery and design using machine learning, *Journal of Materomics.* 3 (2017) 159–177. doi:10.1016/j.jmat.2017.08.002.

[30] H. Abdel-Khalek, M.I. El-Samahi, M.A.- El Salam, A.M. El-Mahalawy, Fabrication and performance evaluation of ultraviolet photodetector based on organic /inorganic heterojunction, *Current Applied Physics.* 18 (2018) 1496–1506. doi:10.1016/j.cap.2018.09.006.

[31] S.M. Stigler, Regression towards the mean, historically considered, *Stat. Methods Med. Res.* 6 (1997) 103–114. doi:10.1177/096228029700600202.

[32] J.M. Stanton, Galton, Pearson, and the Peas: A Brief History of Linear Regression for Statistics Instructors, *J. Stat. Educ.* 9 (2001). doi:10.1080/10691898.2001.11910537.

[33] T. Hastie, R. Tibshirani, J. Friedman, Linear Methods for Regression, in: 2009: pp. 43–99. doi:10.1007/978-0-387-84858-7_3.

[34] E. Ostertagová, Modelling using polynomial regression, in: *Procedia Eng.*, 2012: pp. 500–506. doi:10.1016/j.proeng.2012.09.545.

[35] R. de Vlaming, P.J.F. Groenen, The Current and Future Use of Ridge Regression for Prediction in Quantitative Genetics, *Biomed Res. Int.* 2015 (2015) 1–18. doi:10.1155/2015/143712.

[36] N.R. Draper, R.C. van Nostrand, Ridge Regression and James-Stein Estimation: Review and Comments, *Technometrics.* 21 (1979) 451. doi:10.2307/1268284.

[37] M.G. USAI, M.E. GODDARD, B.J. HAYES, LASSO with cross-validation for genomic selection, *Genet. Res. (Camb).* 91 (2009) 427–436. doi:10.1017/S0016672309990334.

[38] H. Ismanto, R. Wardoyo, Analysis of C4 . 5 and K-Nearest Neighbor (KNN) Method on Algorithm of Clustering For Deciding Mainstay Area, *IOSR J. Comput. Eng.* 18 (2016) 86–92. doi:10.9790/0661-1802048692.

[39] N.S. Altman, An introduction to kernel and nearest-neighbor nonparametric regression, *Am. Stat.* 46 (1992) 175–185. doi:10.1080/00031305.1992.10475879.

[40] N. Kumar, L. Zhang, S. Nayar, What Is a Good Nearest Neighbors Algorithm for Finding Similar Patches in Images?, in: D. Forsyth, P. Torr, A. Zisserman (Eds.), *Computer Vision – ECCV 2008*, Springer Berlin Heidelberg, 2008: pp. 364–378.

[41] G. Biau, Analysis of a Random Forests Model, *J. Mach. Learn. Res.* 13 (2012) 1063–1095. <http://dl.acm.org/citation.cfm?id=2503308.2343682> (accessed October 5, 2019).

[42] L. Breiman, Random Forests, *Mach. Learn.* 45 (2001) 5–32. doi:10.1023/A:1010933404324.

[43] T. Hastie, R. Tibshirani, J. Friedman, Random Forests, in: 2009: pp. 587–604. doi:10.1007/978-0-387-84858-7_15.

[44] H. Drucker, C.J.C. Burges, L. Kaufman, A. Smola, V. Vapnik, Support Vector Regression Machines, in: *ADVANCES IN NEURAL INFORMATION PROCESSING SYSTEMS 9*, MIT Press, 1997: pp. 155–161. doi=10.1.1.21.5909.

[45] A.J. Smola, B. Schölkopf, A Tutorial on Support Vector Regression, *Statistics and Computing.* 14 (2004) 199–222. doi:10.1023/B:STCO.0000035301.49549.88.

[46] T. Hastie, R. Tibshirani, J. Friedman, Prototype Methods and Nearest-Neighbors, in: 2009: pp. 459–483. doi:10.1007/978-0-387-84858-7_13.

[47] M. Pelillo, Alhazen and the nearest neighbor rule, *Pattern Recognit. Lett.* 38 (2014) 34–37. doi:10.1016/j.patrec.2013.10.022.

[48] C.D. Manning, P. Raghavan, H. Schütze, *Introduction to Information Retrieval*, Cambridge University Press, New York, NY, USA, 2008. <https://dl.acm.org/citation.cfm?id=1394399>.

[49] R.F. Sproull, Refinements to nearest-neighbor searching in k -dimensional trees, *Algorithmica* 6 (1991) 579–589. doi:10.1007/BF01759061.

[50] J.L. Bentley, Multidimensional Binary Search Trees Used for Associative Searching, *Commun. ACM*. 18 (1975) 509–517. doi:10.1145/361002.361007.

[51] A. Golbraikh, A. Tropsha, Beware of $q^2!$, *J. Mol. Graph. Model.* 20 (2002) 269–276. doi:10.1016/S1093-3263(01)00123-1.

[52] T. Hastie, R. Tibshirani, J. Friedman, *Neural Networks*, in: 2009: pp. 389–416. doi:10.1007/978-0-387-84858-7_11.

[53] R. Lippmann, An introduction to computing with neural nets, *IEEE ASSP Magazine*. 4 (1987) 4–22. doi:10.1109/MASSP.1987.1165576.

[54] B. Karlik, A.V. Olgac, Performance Analysis of Various Activation Functions in Generalized MLP Architectures o, *Journal of Artificial Intelligence and Expert Systems*. (2010) 111–122.

[55] X. Glorot, Y. Bengio, Understanding the difficulty of training deep feedforward neural networks, in: Y.W. Teh, M. Titterington (Eds.), *Proceedings of the Thirteenth International Conference on Artificial Intelligence and Statistics*, PMLR, Chia Laguna Resort, Sardinia, Italy, 2010: pp. 249–256. <http://proceedings.mlr.press/v9/glorot10a.html>.

[56] K. Hornik, M. Stinchcombe, H. White, Multilayer feedforward networks are universal approximators, *Neural Networks*. 2 (1989) 359–366. doi:10.1016/0893-6080(89)90020-8.

[57] M.R. Baker, R.B. Patil, Universal Approximation Theorem for Interval Neural Networks, *Reliable Computing*. 4 (1998) 235–239. doi:10.1023/A:1009951412412.

[58] D. Stathakis, How many hidden layers and nodes?, *International Journal of Remote Sensing*. 30 (2009) 2133–2147. doi:10.1080/01431160802549278.

[59] B. Curry, P. Morgan, Model selection in Neural Networks: Some difficulties, *European Journal of Operational Research*. 170 (2006) 567–577. doi:10.1016/j.ejor.2004.05.026.

[60] R. Reed, Pruning Algorithms-a Survey, *Trans. Neur. Netw.* 4 (1993) 740–747. doi:10.1109/72.248452.

[61] R. Rojas, R. Rojas, The Backpropagation Algorithm, in: *Neural Networks*, Springer Berlin Heidelberg, Berlin, Heidelberg, 2011: pp. 149–182. doi:10.1007/978-3-642-61068-4_7.

[62] D.E. Rumelhart, G.E. Hinton, R.J. Williams, Learning representations by back-propagating errors, *Nature*. 323 (1986) 533–536. doi:10.1038/323533a0.

[63] D.P. Kingma, J. Ba, Adam: A Method for Stochastic Optimization, ArXiv:1412.6980 [Cs.LG]. (2014). <http://arxiv.org/abs/1412.6980>.

[64] X. Glorot, A. Bordes, Y. Bengio, Deep Sparse Rectifier Neural Networks, in: G. Gordon, D. Dunson, M. Dudík (Eds.), *Proceedings of the Fourteenth International Conference on Artificial Intelligence and Statistics*, PMLR, Fort Lauderdale, FL, USA, 2011: pp. 315–323. <http://proceedings.mlr.press/v15/glorot11a.html>.

[65] F. Chollet, others, Keras, (2015). <https://github.com/fchollet/keras>.

[66] Q. Yao, M. Wang, Y. Chen, W. Dai, H. Yi-Qi, L. Yu-Feng, T. Wei-Wei, Y. Qiang, Y. Yang, Taking Human out of Learning Applications: A Survey on Automated Machine Learning, ArXiv:1810.13306 [Cs, Stat]. (2018). <http://arxiv.org/abs/1810.13306> (accessed October 5, 2019).

[67] R.S. Olson, J.H. Moore, TPOT: A Tree-Based Pipeline Optimization Tool for Automating Machine Learning, in: F. Hutter, L. Kotthoff, J. Vanschoren (Eds.), *Automated Machine Learning: Methods, Systems, Challenges*, Springer International Publishing, Cham, 2019: pp. 151–160. doi:10.1007/978-3-030-05318-5_8.

[68] W. Banzhaf, F.D. Francone, R.E. Keller, P. Nordin, Genetic programming : an introduction on the automatic evolution of computer programs and its applications, Morgan Kaufmann Publishers, 1998. <https://dl.acm.org/citation.cfm?id=280485>.

[69] F.-A. Fortin, F.-M.D. Rainville, M.-A. Gardner, M. Parizeau, C. Gagné, DEAP: Evolutionary Algorithms Made Easy, *J. Mach. Learn. Res.* 13 (2012) 2171–2175. <http://www.jmlr.org/papers/v13/fortin12a.html>.

[70] D. Zeidler, S. Frey, K.-L. Kompa, M. Motzkus, Evolutionary algorithms and their application to optimal control studies, *Phys. Rev. A.* 64 (2001) 023420. doi:10.1103/PhysRevA.64.023420.

[71] T. Chen, C. Guestrin, XGBoost: A Scalable Tree Boosting System, in: *Proceedings of the 22Nd ACM SIGKDD International Conference on Knowledge Discovery and Data Mining*, ACM, New York, NY, USA, 2016: pp. 785–794. doi:10.1145/2939672.2939785.

[72] J. Preskill, Quantum Computing in the NISQ era and beyond, *Quantum.* 2 (2018) 79. doi:10.22331/q-2018-08-06-79.

[73] U.L. Andersen, J.S. Neergaard-Nielsen, P. Van Loock, A. Furusawa, Hybrid discrete- and continuous-variable quantum information, *Nat. Phys.* 11 (2015) 713–719. doi:10.1038/nphys3410.

[74] V. Bergholm, J. Izaac, M. Schuld, C. Gogolin, C. Blank, K. McKiernan, N. Killoran, PennyLane: Automatic differentiation of hybrid quantum-classical computations, *ArXiv:1811.04968 [Physics, Physics:Quant-Ph].* (2018). <http://arxiv.org/abs/1811.04968> (accessed June 19, 2019).

[75] J.R. McClean, J. Romero, R. Babbush, A. Aspuru-Guzik, The theory of variational hybrid quantum-classical algorithms, *New J. Phys.* 18 (2016). doi:10.1088/1367-2630/18/2/023023.

[76] M.A. Nielsen, I.L. Chuang, *Quantum computation and quantum information*, Cambridge University Press, 2010.

[77] G. Adesso, S. Ragy, A.R. Lee, Continuous Variable Quantum Information: Gaussian States and Beyond, *Open Syst. Inf. Dyn.* 21 (2014) 1440001. doi:10.1142/S1230161214400010.

[78] U.L. Andersen, G. Leuchs, C. Silberhorn, Continuous-variable quantum information processing, *Laser Photonics Rev.* 4 (2010) 337–354. doi:10.1002/lpor.200910010.

[79] C.H. Bennett, D.P. DiVincenzo, Quantum information and computation, *Nature.* 404 (2000) 247–255. doi:10.1038/35005001.

[80] N. Liu, J. Thompson, C. Weedbrook, S. Lloyd, V. Vedral, M. Gu, K. Modi, Power of one qumode for quantum computation, *Phys. Rev. A.* 93 (2016) 052304. doi:10.1103/PhysRevA.93.052304.

[81] M. Schuld, F. Petruccione, Quantum Information, in: 2018: pp. 75–125. doi:10.1007/978-3-319-96424-9_3.

[82] S. Olivares, Quantum optics in the phase space, *Eur. Phys. J. Spec. Top.* 203 (2012) 3–24. doi:10.1140/epjst/e2012-01532-4.

[83] C. Weedbrook, S. Pirandola, R. García-Patrón, N.J. Cerf, T.C. Ralph, J.H. Shapiro, S. Lloyd, Gaussian quantum information, *Rev. Mod. Phys.* 84 (2012) 621–669. doi:10.1103/RevModPhys.84.621.

[84] E. Schrödinger, An Undulatory Theory of the Mechanics of Atoms and Molecules, *Phys. Rev.* 28 (1926) 1049–1070. doi:10.1103/PhysRev.28.1049.

[85] S. Lloyd, S.L. Braunstein, Quantum Computation over Continuous Variables, *Phys. Rev. Lett.* 82 (1999) 1784–1787. doi:10.1103/PhysRevLett.82.1784.

[86] N. Killoran, T.R. Bromley, J.M. Arrazola, M. Schuld, N. Quesada, S. Lloyd, Continuous-variable quantum neural networks, *ArXiv:1806.06871 [Quant-Ph].* (2018). <http://arxiv.org/abs/1806.06871> (accessed June 18, 2019).

[87] M. Oszmaniec and Z. Zimboras, Universal Extensions of Restricted Classes of Quantum Operations, *Phys. Rev. Lett.* 119 (2017) 220502. doi.org/10.1103/PhysRevLett.119.220502

[88] S.L. Braunstein, P. van Loock, Quantum information with continuous variables, (2004). doi:10.1103/RevModPhys.77.513.

[89] V.V. Dodonov, ‘Nonclassical’ states in quantum optics: a ‘squeezed’ review of the first 75 years, *J. Opt. B Quantum Semiclassical Opt.* 4 (2002) R1–R33. doi:10.1088/1464-4266/4/1/201.

[90] Z.R. Gong, H. Ian, Y. Liu, C.P. Sun, F. Nori, Effective Hamiltonian approach to the Kerr nonlinearity in an optomechanical system, *Phys. Rev. A.* 80 (2009) 065801. doi:10.1103/PhysRevA.80.065801.

[91] K.B. Mo/lle, T.G. Jo/rgensen, J.P. Dahl, Displaced squeezed number states: Position space representation, inner product, and some applications, *Phys. Rev. A.* 54 (1996) 5378–5385. doi:10.1103/PhysRevA.54.5378.

[92] M.M. Nieto, Displaced and Squeezed Number States, *Physics Letters A.* 229 (1997) 135–143. doi:10.1016/S0375-9601(97)00183-7.

[93] V. Havlíček, A.D. Cárocoles, K. Temme, A.W. Harrow, A. Kandala, J.M. Chow, J.M. Gambetta, Supervised learning with quantum-enhanced feature spaces, *Nature*. 567 (2019) 209–212. doi:10.1038/s41586-019-0980-2.

[94] M. Schuld, N. Killoran, Quantum Machine Learning in Feature Hilbert Spaces, *Phys. Rev. Lett.* 122 (2019) 040504. doi:10.1103/PhysRevLett.122.040504.

[95] M. Schuld, F. Petruccione, Supervised Learning with Quantum Computers, 2018. doi:10.1007/978-3-319-96424-9.

[96] P. Wittek, Quantum Machine Learning: What Quantum Computing Means to Data Mining, 2014.

[97] V.V. Dodonov, V.I. Man’ko, V.I. Man’ko, Theory of Nonclassical States of Light, CRC Press, 2003. doi:10.1201/9781482288223.

[98] V.V. Dodonov, O.V. Man’ko, V.I. Man’ko, A. Wünsche, Hilbert-Schmidt distance and non-classicality of states in quantum optics, *Journal of Modern Optics*. 47 (2000) 633–654. doi:10.1080/09500340008233385.

[99] M. Schuld, V. Bergholm, C. Gogolin, J. Izaac, N. Killoran, Evaluating analytic gradients on quantum hardware, *Phys. Rev. A*. 99 (2019) 032331. doi:10.1103/PhysRevA.99.032331.

[100] N. Ghobadi, Band gap determination using absorption spectrum fitting procedure, *Int Nano Lett.* 3 (2013) 2. doi:10.1186/2228-5326-3-2.

[101] A.M. Nawar, A.M. El-Mahalawy, Simple processed semi-transparent Schottky diode based on PMMA-MWCNTs nanocomposite for new generation of optoelectronics, *Synthetic Metals*. 255 (2019) 116102. doi:10.1016/j.synthmet.2019.116102.

[102] S.K. Lai, L. Tang, Y.Y. Hui, C.M. Luk, S.P. Lau, A deep ultraviolet to near-infrared photore-sponse from glucose-derived graphene oxide, *J. Mater. Chem. C*. 2 (2014) 6971–6977. doi:10.1039/C4TC01175A.

[103] A.G. Imer, Y.S. Ocak, Effect of Light Intensity and Temperature on the Current Voltage Char-acteristics of Al/SY/p-Si Organic–Inorganic Heterojunction, *Journal of Elec Materi*. 45 (2016) 5347–5355. doi:10.1007/s11664-016-4649-4.

[104] J. Lee, T. Uhrmann, T. Dimopoulos, H. Bruckl, J. Fidler, TEM Study on Diffusion Process of NiFe Schottky and MgO/NiFe Tunneling Diodes for Spin Injection in Silicon, *IEEE Transac-tions on Magnetics*. 46 (2010) 2067–2069. doi:10.1109/TMAG.2010.2040594.

[105] N. Maity, R. Maity, R. Thapa, S. Baishya, Image Force Effect on Tunneling Current for Ultra Thin High-K Dielectric Material Al₂O₃ Based Metal Oxide Semiconductor Devices, *Journal of Nanoelectronics and Optoelectronics*. 10 (2015). doi:10.1166/jno.2015.1812.

[106] M.A. Mayimele, J.P.J. van Rensburg, F.D. Auret, M. Diale, Analysis of temperature-dependant current–voltage characteristics and extraction of series resistance in Pd/ZnO Schottky barrier diodes, *Physica B: Condensed Matter*. 480 (2016) 58–62. doi:10.1016/j.physb.2015.07.034.

[107] M.M. El-Nahass, H.S. Metwally, H.E.A. El-Sayed, A.M. Hassanien, Electrical and photovoltaic properties of FeTPPCL/p-Si heterojunction, *Synthetic Metals*. 161 (2011) 2253–2258. doi:10.1016/j.synthmet.2011.08.030.

[108] H. Abdel-Khalek, E. Shalaan, M. Abd-El Salam, A.M. El-Mahalawy, Effect of illumination in-tensity on the characteristics of Cu(acac)₂/n-Si photodiode, *Synthetic Metals*. 245 (2018) 223–236. doi:10.1016/j.synthmet.2018.09.009.

[109] V. Aubry, F. Meyer, Schottky diodes with high series resistance: Limitations of forward I-V methods, *Journal of Applied Physics*. 76 (1994) 7973–7984. doi:10.1063/1.357909.

[110] H. Norde, A modified forward I-V plot for Schottky diodes with high series resistance, *Journal of Applied Physics*. 50 (1979) 5052–5053. doi:10.1063/1.325607.

[111] K. Sato, Y. Yasumura, Study of forward I-V plot for Schottky diodes with high series resistance, *Journal of Applied Physics*. 58 (1985) 3655–3657. doi:10.1063/1.335750.

[112] S.C. Roy, T. Kundu, V.R. Rao, Illumination effect on electrical characteristics of pristine PVA based broadband photodetector, in: 2015 IEEE 15th International Conference on Nanotechnol-ogy (IEEE-NANO), 2015: pp. 362–365. doi:10.1109/NANO.2015.7389001.

[113] H.M. Zeyada, M.I. Youssif, N.A. El-Ghamaz, M.A. Nasher, Carrier transport mechanisms and photovoltaic characteristics of Au/toluidine blue/n-Si/Al heterojunction solar cell, *J Mater Sci: Mater Electron*. 29 (2018) 3592–3601. doi:10.1007/s10854-017-8289-0.

[114] A.M. Nawar, M.M. Makhlof, Au-nanoparticles doped SiO₂ interfacial layer to promote the photovoltaic characteristics of Au/p-Si/Al solar cells, *Journal of Alloys and Compounds*. 767 (2018) 1271–1281. doi:10.1016/j.jallcom.2018.09.104.

[115] P.K. Nayak, N. Periasamy, Calculation of electron affinity, ionization potential, transport gap, optical band gap and exciton binding energy of organic solids using ‘solvation’ model and DFT, *Organic Electronics*. 10 (2009) 1396–1400. doi:10.1016/j.orgel.2009.06.011.

[116] J. Zhou, J. Huang, Photodetectors Based on Organic–Inorganic Hybrid Lead Halide Perovskites, *Advanced Science*. 5 (2018) 1700256. doi:10.1002/advs.201700256.

[117] Y. Li, C.-Y. Xu, J.-Y. Wang, L. Zhen, Photodiode-Like Behavior and Excellent Photoresponse of Vertical Si/Monolayer MoS₂ Heterostructures, *Scientific Reports*. 4 (2014) 7186. doi:10.1038/srep07186.

[118] T.-F. Zhang, G.-A. Wu, J.-Z. Wang, Y.-Q. Yu, D.-Y. Zhang, D.-D. Wang, J.-B. Jiang, J.-M. Wang, L.-B. Luo, A sensitive ultraviolet light photodiode based on graphene-on-zinc oxide Schottky junction, *Nanophotonics*. 6 (2017) 1073–1081. doi:10.1515/nanoph-2016-0143.

[119] X. Gong, M. Tong, Y. Xia, W. Cai, J.S. Moon, Y. Cao, G. Yu, C.-L. Shieh, B. Nilsson, A.J. Heeger, High-Detectivity Polymer Photodetectors with Spectral Response from 300 nm to 1450 nm, *Science*. 325 (2009) 1665–1667. doi:10.1126/science.1176706.

[120] W. Li, D. Li, G. Dong, L. Duan, J. Sun, D. Zhang, L. Wang, High-stability organic red-light photodetector for narrowband applications, *Laser & Photonics Reviews*. 10 (2016) 473–480. doi:10.1002/lpor.201500279.

[121] H.A. Afify, M.M. El-Nahass, A. –S. Gadallah, M. Atta Khedr, Carrier transport mechanisms and photodetector characteristics of Ag/TiOPc/p-Si/Al hybrid heterojunction, *Materials Science in Semiconductor Processing*. 39 (2015) 324–331. doi:10.1016/j.mssp.2015.05.026.

[122] M. Bednorz, G.J. Matt, E.D. Głowacki, T. Fromherz, C.J. Brabec, M.C. Scharber, H. Sitter, N.S. Sariciftci, Silicon/organic hybrid heterojunction infrared photodetector operating in the telecom regime, *Organic Electronics*. 14 (2013) 1344–1350. doi:10.1016/j.orgel.2013.02.009.

[123] A.A. Attia, M.M. Saadeldin, H.S. Soliman, A.-S. Gadallah, K. Sawaby, Structural and optical properties of p-quaterphenyl thin films and application in organic/inorganic photodiodes, *Optical Materials*. 62 (2016) 711–716. doi:10.1016/j.optmat.2016.10.046.

[124] H. Abd El-Khalek, M. Abd- El Salam, F.M. Amin, Fabrication and characterization of dual-band organic/inorganic photodetector for optoelectronic applications, *Current Applied Physics*. 19 (2019) 629–638. doi:10.1016/j.cap.2019.02.017.

[125] L. Dou, Y. (Micheal) Yang, J. You, Z. Hong, W.-H. Chang, G. Li, Y. Yang, Solution-processed hybrid perovskite photodetectors with high detectivity, *Nature Communications*. 5 (2014) 5404. doi:10.1038/ncomms6404.

[126] F. Pedregosa, G. Varoquaux, A. Gramfort, V. Michel, B. Thirion, O. Grisel, M. Blondel, A. Müller, J. Nothman, G. Louppe, P. Prettenhofer, R. Weiss, V. Dubourg, J. Vanderplas, A. Pas-sos, D. Cournapeau, M. Brucher, M. Perrot, É. Duchesnay, Scikit-learn: Machine Learning in Python, *J. Mach. Learn. Res.* 12 (2012) 2825–2830. <http://www.jmlr.org/papers/v12/pedregosa11a.html> <http://arxiv.org/abs/1201.0490>.

[127] M. Abadi, A. Agarwal, P. Barham, E. Brevdo, Z. Chen, C. Citro, G.S. Corrado, A. Davis, J. Dean, M. Devin, S. Ghemawat, I. Goodfellow, A. Harp, G. Irving, M. Isard, Y. Jia, R. Jozefowicz, L. Kaiser, M. Kudlur, J. Levenberg, D. Mane, R. Monga, S. Moore, D. Murray, C. Olah, M. Schuster, J. Shlens, B. Steiner, I. Sutskever, K. Talwar, P. Tucker, V. Vanhoucke, V. Vasudevan, F. Viegas, O. Vinyals, P. Warden, M. Wattenberg, M. Wicke, Y. Yu, X. Zheng, TensorFlow: Large-Scale Machine Learning on Heterogeneous Distributed Systems, (2016). <http://arxiv.org/abs/1603.04467>.

[128] N. Killoran, J. Izaac, N. Quesada, V. Bergholm, M. Amy, C. Weedbrook, Strawberry Fields: A Software Platform for Photonic Quantum Computing, *Quantum*. 3 (2018) 129. doi:10.22331/q-2019-03-11-129.

[129] A. Rahimi, B. Recht, Random Features for Large-scale Kernel Machines, in: Proceedings of the 20th International Conference on Neural Information Processing Systems, Curran Associates Inc., USA, 2007: pp. 1177–1184. <http://dl.acm.org/citation.cfm?id=2981562.2981710> (accessed October 2, 2019).